Identification of subsurface structures using electromagnetic data and shape priors

Identification of subsurface structures using electromagnetic data and shape priors

Svenn Tveit[a,b,*], Shaaban A. Bakr[c,a], Martha Lien[a,d], Trond Mannseth[a,b]

[a] *Uni CIPR, Uni Research, Bergen 5020, Norway*
[b] *Department of Mathematics, University of Bergen, Bergen 5020, Norway*
[c] *Department of Mathematics, Faculty of Science, Assiut University, Assiut 71516, Egypt*
[d] *Present address: Octio AS, Bøhmergaten 44, Bergen 5057, Norway*

Abstract

We consider the inverse problem of identifying large-scale subsurface structures using the controlled source electromagnetic method. To identify structures in the subsurface where the contrast in electric conductivity can be small, regularization is needed to preserve structural information. We propose to combine two approaches for regularization of the inverse problem. In the first approach we utilize a model-based, reduced, composite representation of the electric conductivity that is highly flexible, even for a moderate number of degrees of freedom. With a low number of parameters, the inverse problem is efficiently solved using a standard, second-order gradient-based optimization algorithm. Further regularization is obtained using structural prior information, available, e.g., from interpreted seismic data. The reduced conductivity representation is suitable for incorporation of structural prior information. Such prior information can, however, not be accurately modeled with a gaussian distribution. To alleviate this, we incorporate the structural information using shape priors. The shape prior technique requires the choice of kernel function, which is application dependent. We argue for using the conditionally positive definite kernel which is shown to have computational advantages over the commonly applied gaussian kernel for our problem. Numerical experiments on various test cases show that the methodology is able to identify fairly complex subsurface electric conductivity distributions while preserving structural prior information during the inversion.

Keywords: Inverse problem, Electric conductivity estimation, Reduced parameterization, Shape priors

1. Introduction

Marine geophysical exploration is important, for example, in the search for new offshore petroleum reservoirs. Several surface methods have been developed to attempt depiction of the subsurface geological structures, and thereby direct or indirect detection of a possible presence of hydrocarbons. The procedure for most surface methods is: transmission of energy into the subsurface; measurement on the surface, and; inversion to get a map of the subsurface physical properties. Over the last decades, seismic reflection methods have been widely used in hydrocarbon exploration, but more recently, electromagnetic methods have also gained interest, particularly controlled source electromagnetics (CSEM), see, e.g., [1] and references therein.

With CSEM, a towed electric dipole transmits low-frequency (0.1-10 Hz) electromagnetic (EM) signals into the subsurface. The transmitted signals are sensitive to the subsurface electric conductivity. The electric conductivities of brine and oil saturated porous media differs by 1-2 orders of magnitude, which makes CSEM attractive as a hydrocarbon indicator. The recorded response in the sea floor receivers is, however, the result of the interaction of the EM signals with a subsurface region much larger than that of

*Corresponding author
Email addresses: svenn.tveit@uni.no (Svenn Tveit), shaaban.bakr1@gmail.com (Shaaban A. Bakr), martha.lien@octio.com (Martha Lien), trond.mannseth@uni.no (Trond Mannseth)

a (potentially existing) petroleum reservoir. The usefulness of CSEM therefore relies on its ability to map the entire subsurface region that is being explored with reasonable accuracy.

Subsurface geology is typically dominated by large-scale structures (geological strata), although subsurface properties also vary within a structure. The main aim with the research presented in this paper is to develop a computationally efficient inversion methodology for CSEM data that is able to preserve prior information about geological strata, and we will therefore apply a model-based representation (see, e.g., [2–9]) of the unknown electric conductivity field. Alternatively, a pixel-based representation (see, e.g., [10–13]) could have been used, although the tendency for smoothing out the resulting conductivity field makes it less attractive. Additionally, large computational costs are associated with running second-order gradient-based optimization algorithms with a pixel-based representation, due to the large number of parameters.

The majority of subsurface geological strata are brine saturated. Electric conductivity contrasts between different brine saturated strata are typically much weaker than those occurring between a brine saturated stratum and a petroleum reservoir. Data from EM signals which have propagated through the brine saturated strata have low resolution power due to the diffusive nature of the low-frequency EM signals. This makes it very challenging to solve the inverse problem of obtaining correct placement of structure boundaries from CSEM data alone. In addition, there is a possibility of getting trapped in local minima when using gradient-based optimization algorithms, due to nonlinearity in the mapping from conductivity to EM data.

To enhance stability and to reduce model nonlinearity, we apply regularization by reduced parameterization and adjustable smoothing of the structure boundaries, extending the work in [8, 9]. The reduced representation allows for use of Gauss-Newton-type optimization algorithms as the low number of parameters permits the model to be updated using second-order derivative (Hessian) information. To further aid in obtaining accurate placement of structure boundaries, it would be an advantage if structural prior information could be applied. How to achieve this will be a major topic in the paper.

From the inversion methodology viewpoint, it is not crucial where the structural prior information comes from, but it seems natural to point to seismic data in this context. Seismic data are sensitive to elastic properties of the subsurface, and are applied to detect interfaces between geological strata. They are usually interpreted by geologists in combination with well logs and outcrop analogues. The outcome of this process is a set of possible structural subsurface models, from which one model may be selected as the most probable. There is often a fair amount of uncertainty and ambiguity associated with this selection process. Without going into any detail about geological interpretation, we will simply assume that uncertain structural subsurface information exist, and seek to utilize this information to build a prior model for the structural CSEM inversion to increase reliability of the inversion results. We will, however, sometimes refer to the structural prior information as seismic interpretations, etc., for convenience. (Note also that joint inversion of seismic data and CSEM data, see, e.g., [14–17], is an alternative way to utilize the information in seismic data in the context of CSEM inversion.) As a final remark concerning the origin of the structural information, we note that it is not guaranteed that all large-scale structures with respect to elastic properties always correspond exactly to large-scale structures with respect to electric properties. Further discussion of this complex issue is, however, outside the scope of the paper.

Use of prior information in an inversion requires that a prior probability density function (PDF) for the parameters involved in the estimation is specified. A very common assumption for many subsurface-related problems is that the prior PDF is multivariate gaussian. When the solution of the inverse problem is expected to contain several large-scale structures as a dominating feature, like in our case, any realistic prior PDF associated with a pixel-based parameterization would be multimodal, and therefore non-gaussian. We apply an entirely different parameterization, but even so, it is still not clear how to directly design a realistic prior PDF for the parameters involved. Our parameterization does, however, facilitate representation of structural prior information as *training images*, where one training image corresponds to a possible structural subsurface model. Subsequently, the training images are used to build a (not necessarily gaussian) PDF for the subsurface structures that is incorporated in the inversion methodology as a *shape prior* [18]. Shape priors allow for calculation of non-gaussian PDF's by transforming them to a space where they follow a gaussian distribution. The calculation requires a choice of *kernel function*, which to some degree is application dependent, with the gaussian kernel being the common choice. We will, however, argue for the use of a conditionally positive definite kernel [19], as it is shown to aid the gradient-based algorithm in a

favorable manner compared to the gaussian kernel.

The paper is organized as follows: In section 2, we describe the numerical solver for Maxwell's equations. The formulation of the inverse problem is outlined in section 3. This includes a description of the parameter representation in section 3.1, and a discussion of shape priors and kernel functions in section 3.2. A description of the procedure for solving the optimization problem is given in section 4. In section 5, we present numerical results involving various types of subsurface geological structures, where we demonstrate the performance of the novel inversion methodology. The main aim of the numerical investigation is to assess the importance of using structural prior information for achieving CSEM inversion results that preserves geological strata. We end with some concluding remarks in section 6.

2. Forward model

The subsurface propagation of EM waves is governed by Maxwell's equations. Stated in the frequency domain, they are

$$\nabla \times \mathbf{e} - \mathrm{i}\omega\mu\mathbf{h} = 0, \tag{1}$$
$$\nabla \times \mathbf{h} - \sigma\mathbf{e} = \mathbf{j}, \tag{2}$$
$$\nabla \cdot (\epsilon\mathbf{e}) = 0, \tag{3}$$
$$\nabla \cdot (\mu\mathbf{h}) = 0, \tag{4}$$

where we have assumed a time harmonic convention $\mathrm{e}^{-\mathrm{i}\omega t}$, with ω denoting angular frequency and $\mathrm{i} = \sqrt{-1}$. We have also assumed no free electric charges, and neglected displacement currents due to low frequency signals. In (1) - (4), $\mathbf{e}$ and $\mathbf{h}$ are the electric and magnetic fields, respectively, $\mathbf{j}$ is the electric source current distribution, ϵ denotes the permittivity, μ denotes the magnetic permeability, and σ denotes the electric conductivity (assumed to be isotropic). Taking the curl of (1) and using (2) we can eliminate $\mathbf{h}$, yielding

$$\nabla \times \left(\mu^{-1}\nabla \times \mathbf{e}\right) - \mathrm{i}\omega\sigma\mathbf{e} = \mathrm{i}\omega\mathbf{j}. \tag{5}$$

If desired, $\mathbf{h}$ can be found from (1) when $\mathbf{e}$ is known. In this paper, we only consider the electric field responses.

The diffusive nature of EM waves in the subsurface implies that the EM fields go to zero at infinity for an unbounded domain. On a finite computational domain, $\Omega \in \mathbb{R}^3$, we therefore impose the condition:

$$\mathbf{e} \times \mathbf{n} \,|_{\partial\Omega} = \mathbf{0}, \tag{6}$$

where $\mathbf{n}$ is a unit normal vector. For (6) to hold, we need $\partial\Omega$ to be sufficiently far away from the area of interest.

2.1. 2.5D formulation

To solve (5), we first write it in variational form following standard procedures. We pre-multiply (5) with the adjoint of an arbitrary test function $\boldsymbol{\kappa}$ before integrating over the domain Ω, which results in the equation

$$\int_\Omega \boldsymbol{\kappa}^* \left(\nabla \times \left(\mu^{-1}\nabla \times \mathbf{e}\right)\right) \mathrm{d}\Omega - \mathrm{i}\omega \int_\Omega \boldsymbol{\kappa}^* \sigma\mathbf{e} \,\mathrm{d}\Omega = \mathrm{i}\omega \int_\Omega \boldsymbol{\kappa}^* \mathbf{j} \,\mathrm{d}\Omega. \tag{7}$$

We define the vector space $\mathcal{H}(\mathrm{curl}) = \left\{\boldsymbol{\kappa} \in \left(\mathcal{L}_2(\Omega)\right)^3 \,|\nabla \times \boldsymbol{\kappa} \in \left(\mathcal{L}_2(\Omega)\right)^3\right\}$ and let the test function be chosen such that

$$\boldsymbol{\kappa} \in \mathcal{H}_{\partial\Omega}(\mathrm{curl}) = \{\boldsymbol{\kappa} \in \mathcal{H}(\mathrm{curl}) \mid (\boldsymbol{\kappa} \times \mathbf{n}) = 0 \text{ on } \partial\Omega\}. \tag{8}$$

Using Green's theorem, we can transform the first integral in (7) as follows:

$$\int_\Omega \boldsymbol{\kappa}^* \left(\nabla \times \left(\mu^{-1}\nabla \times \mathbf{e}\right)\right) \mathrm{d}\Omega = \int_\Omega (\nabla \times \boldsymbol{\kappa})^* \left(\mu^{-1}\nabla \times \mathbf{e}\right) \mathrm{d}\Omega. \tag{9}$$

Inserting the identity (9) into (7) we get the variational form of (5) given as

$$\left\langle \nabla \times \boldsymbol{\kappa}, \mu^{-1} \nabla \times \mathbf{e} \right\rangle - \mathrm{i}\omega \left\langle \boldsymbol{\kappa}, \sigma \mathbf{e} \right\rangle = \mathrm{i}\omega \left\langle \boldsymbol{\kappa}, \mathbf{j} \right\rangle, \tag{10}$$

where $\langle \cdot, \cdot \rangle$ denote the standard $\mathcal{L}_2$ inner product.

Solving the full 3D problem can be computationally expensive, especially in an inversion setting. To overcome this challenge we apply a 2.5D formulation of the problem [20]. This means that the field components, $\mathbf{e}$ and $\mathbf{j}$, are functions of x, y and z, while the electric conductivity, σ, is only a function of x and z; thus y is defined as the strike direction. The splitting is done through a 1D Fourier transformation along the strike direction, y, defined as

$$\hat{\mathbf{f}}(x, \xi, z) \equiv \frac{1}{\sqrt{2\pi}} \int_{\mathbb{R}} \mathbf{f}(x, y, z)\, \mathrm{e}^{-\mathrm{i}\xi y}\, \mathrm{d}y, \tag{11}$$

where ξ denotes the Fourier mode. By Fourier transforming (10) we get a sequence of independent 2D problems (one for each Fourier mode) to solve in $\Omega_{\mathrm{2D}} \in \mathbb{R}^2$. Hence, we reduce the computational cost significantly compared to solving the full 3D problem.

2.2. Finite element solution

We discretize the computational domain Ω_{2D} into triangular elements using Triangle [21], and solve the 2.5D problem with the finite element method (FE). Ultimately, the result of the FE formulation can be written as a linear system

$$\mathbf{A}\hat{\mathbf{e}} = \hat{\mathbf{b}}, \tag{12}$$

where $\mathbf{A}$ denotes the stiffness matrix, $\hat{\mathbf{e}}$ is the Fourier transformed electric field in Ω_{2D} and $\hat{\mathbf{b}}$ is the discrete counterpart of the source term (right-hand side) in (10). We solve (12) using LU decomposition. Subsequently, we pick out the Fourier transformed electric field components at the centroid of the triangles containing the receivers using linear interpolation. Lastly, we use the inverse Fourier transform, defined as

$$\mathbf{f}(x, y, z) \equiv \frac{1}{\sqrt{2\pi}} \int_{\mathbb{R}} \hat{\mathbf{f}}(x, \xi, z)\, \mathrm{e}^{\mathrm{i}\xi y}\, \mathrm{d}\xi, \tag{13}$$

to apprehend the actual electric field components. This integral is approximated using the midpoint rule. Further details can be found in [22].

3. Inverse problem

We want to map the subsurface conductivity distribution based on EM data gathered at the receiver positions for exploration purposes. We introduce a data vector $\tilde{\mathbf{d}} \in \mathbb{C}^{N_{\mathrm{D}}}$ containing the electric field responses observed at the receiver positions:

$$\tilde{\mathbf{d}} = \left[\tilde{d}_1, \tilde{d}_2, ...\tilde{d}_{N_{\mathrm{D}}}\right]^T. \tag{14}$$

The superscript T denotes matrix or vector transpose and N_{D} is the number of measurements. The electric field at the receivers calculated by the forward model can be summarized in an operator $\tilde{\mathbf{m}}(p) \in \mathbb{C}^{N_{\mathrm{D}}}$, where $p(\mathbf{r}) \in \mathbb{R}^{N_{\mathrm{g}}}$ is a pixel-based representation (i.e. constant within each element) of the subsurface conductivity distribution with N_{g} being the number of grid cells in the inversion domain $D \subseteq \Omega_{\mathrm{2D}}$ and $\mathbf{r} = (x, z)$. For the inversion process, the real and imaginary components of $\tilde{\mathbf{d}}$ and $\tilde{\mathbf{m}}$ are considered (another common choice is amplitude and phase). To this end, let a new set of vectors, $\mathbf{d} \in \mathbb{R}^{N_d}$ and $\mathbf{m}(p) \in \mathbb{R}^{N_d}$, be defined as

$$\mathbf{d} = \begin{bmatrix} \mathrm{Re}(\tilde{\mathbf{d}}) \\ \mathrm{Im}(\tilde{\mathbf{d}}) \end{bmatrix}, \quad \mathbf{m}(p) = \begin{bmatrix} \mathrm{Re}(\tilde{\mathbf{m}}(p)) \\ \mathrm{Im}(\tilde{\mathbf{m}}(p)) \end{bmatrix}, \tag{15}$$

where Re and Im denote the real and imaginary parts of the argument, respectively, and $N_d = 2N_D$.

We can write the mapping between $\mathbf{m}(p)$ and $\mathbf{d}$ as

$$\mathbf{d} = \mathbf{m}(p) + \boldsymbol{\delta}, \tag{16}$$

where $\boldsymbol{\delta} \in \mathbb{C}^{N_\mathrm{d}}$ could include both model and measurement errors. Model errors will, however, not be considered in this paper. Hence we want the predicted responses to correspond to the data up to an order determined by the error term, $\boldsymbol{\delta}$. The limited resolution of CSEM data makes this problem ill-posed. In this paper, we focus on two regularization methods: *reduced parameterization* and *shape priors*.

Reduced parameterization of the unknown parameter function (also called 'regularization by projection' and 'regularization by discretization', see, e.g., [23]), aims to find a low dimensional representation of p (denoted q, here) which corresponds well with the information available about the problem at hand. Shape priors (see, e.g., [18]) allows for incorporation of prior knowledge about subsurface structures as a penalty term (denoted J_prior, here) in the objective function to be minimized,

$$O(q) = J_\mathrm{data}(q) + \beta J_\mathrm{prior}(q). \tag{17}$$

Here, J_data denotes the data misfit function

$$J_\mathrm{data}(q) = (\mathbf{m}(q) - \mathbf{d})^H \mathbf{C}^{-1} (\mathbf{m}(q) - \mathbf{d}), \tag{18}$$

where superscript H denotes the Hermitian, and $\mathbf{C}$ is a diagonal matrix containing estimates of the variance of the data noise. As with any regularization method, reduced parameterization and shape priors will bias the solution. To ensure that the applied regularization does not restrict attainable structure shapes too much, we use a representation of the conductivity which is flexible with respect to the shapes it can represent, even when using a moderate number of parameters. This representation is a further development of the method presented in [8, 9].

3.1. Parameter representation

A parameterized representation of p can be written as a linear basis expansion

$$q(\mathbf{r}; \mathbf{c}, \mathbf{a}) = \sum_{j=1}^{N_\mathrm{c}} c_j(\mathbf{r}) \Psi_j(\mathbf{r}; \mathbf{a}), \tag{19}$$

where $\{\Psi_j\}_{j=1}^{N_\mathrm{c}}$ are the basis functions and $\mathbf{c} = [c_1, c_2, \ldots, c_{N_\mathrm{c}}]^T$ are the corresponding expansion coefficients. Changing c_j will change the value of q on $\mathrm{supp}\Psi_j$, while the vector $\mathbf{a} = [a_1, a_2, \ldots, a_{N_\mathrm{a}}]^T$ can be applied to change the shape and support of the basis functions during the estimation. If $(N_\mathrm{c} + N_\mathrm{a}) < N_\mathrm{g}$, q represents a reduced parameterization of p with respect to a pixel-based representation.

If $\mathbf{c}$ is independent of $\mathbf{r}$, and if $\{\Psi_j\}_{j=1}^{N_\mathrm{c}}$ have non-overlapping support, (19) corresponds to a zonation of D. If, in addition, $\{\Psi_j\}_{j=1}^{N_\mathrm{c}}$ are independent of $\mathbf{a}$, (19) represents zonation with fixed zones, that is, a standard zonation. The parameterization we apply in this paper can largely be seen as an extension of a non-standard zonation – the Vese-Chan level set representation [24], see also [25, 26]. We therefore first describe the basics of that representation, before discussing how our representation, although similar, differs from it.

With a level set representation, zone boundaries are not represented explicitly – rather they are derived from higher dimensional functions, which in turn are represented explicitly. While the level set representation is unique for $N_\mathrm{c} = 2$, different level set representations have been proposed for $N_\mathrm{c} > 2$. Among these, the Vese-Chan level set representation is the more commonly applied. For more details about alternative level set representations and the level set method [27] in general, we refer to the review papers [28–30]. Note also that a level set representation where dependency of $\mathbf{c}$ on $\mathbf{r}$ is accounted for, has been proposed in [6, 31].

3.1.1. Vese-Chan level set representation

The Vese-Chan level set representation is obtained by defining Ψ_j by

$$\Psi_j(\mathbf{r};\mathbf{a}) = \prod_{i=1}^{N_\mathrm{I}} E_j(I_i(\mathbf{r};\mathbf{a})), \tag{20}$$

where

$$E_j(I_i) = \begin{cases} H(I_i), & \text{if } b_j^i = 0, \\ 1 - H(I_i), & \text{if } b_j^i = 1, \end{cases} \tag{21}$$

and where H is the Heaviside function. The symbol b_j^i denotes element no. i in the N_I-dimensional binary representation of $(j-1)$, $\mathrm{bin}(j-1) = \left[b_j^1, b_j^2, \ldots, b_j^{N_\mathrm{I}}\right]$, for $j = 1, 2, \ldots, N_\mathrm{c}$, and N_c is the number of unique numbers that can be represented by N_I binary digits. With $N_\mathrm{I} = 1$, $N_\mathrm{c} = 2$, and (19) reduces to

$$\begin{aligned} q(\mathbf{r};\mathbf{c},\mathbf{a}) &= c_1 E_1(I_1(\mathbf{r};\mathbf{a})) + c_2 E_2(I_1(\mathbf{r};\mathbf{a})) \\ &= c_1 H(I_1(\mathbf{r};\mathbf{a})) + c_2(1 - H(I_1(\mathbf{r};\mathbf{a}))). \end{aligned} \tag{22}$$

In this case, D is split into two regions/zones, where $q = c_1$ in the zone where $I_1 > 0$, $q = c_2$ in the zone where $I_1 < 0$, and the zone boundary is given by the zero level set of the function $I_1(\mathbf{r};\mathbf{a})$ – the level set function.

With $N_\mathrm{I} > 1$, zone boundaries are still given by the zero level sets of the level set functions $\{I_i\}_{i=1}^{N_\mathrm{I}}$, but there will be more than two regions. In general, it is possible to represent $N_\mathrm{c} = 2^{N_\mathrm{I}}$ regions with N_I level set functions, but the actual number of regions that will occur in a particular case, M, depends on the relative configurations of the different zero level sets, $\{I_i^0\}_{i=1}^{N_\mathrm{I}}$. This influence of the zero-level-set geometries is most conveniently illustrated for the case of $N_\mathrm{I} = 2$, in which case (19) reads

$$\begin{aligned} q(\mathbf{r};\mathbf{c},\mathbf{a}) &= c_1 H(I_1) H(I_2) + c_2 H(I_1)(1 - H(I_2)) \\ &\quad + c_3(1 - H(I_1)) H(I_2) + c_4(1 - H(I_1))(1 - H(I_2)), \end{aligned} \tag{23}$$

when suppressing the dependencies of the level set functions on $\mathbf{r}$ and $\mathbf{a}$, for convenience. (A more detailed derivation of (23) is provided in Appendix A.) The zone geometries resulting from selecting a single (arbitrary) configuration of I_2^0, and two different configurations of I_1^0, are shown in Fig. 1. The + and − signs on the plots indicate on which side of the zero level sets the level set functions are positive and negative, respectively. Utilizing the definition of the Heaviside function, q may be evaluated, resulting in $q = c_j$ in region no. j. In Fig. 1a, I_1^0 intersects I_2^0, and there are four regions. In Fig. 1b, I_1^0 and I_2^0 do not intersect, resulting in three regions. With the latter configuration of I_1^0 and I_2^0, region no. 3 has vanished since $\mathrm{supp}\Psi_3 = \mathrm{supp}((1 - H(I_1)) H(I_2)) = \emptyset$. In the general case, $N_\mathrm{I} + 1 \leq M \leq 2^{N_\mathrm{I}}$, where the lower/upper bound corresponds to cases where none/all of the zero level sets intersect, respectively.

The discussion so far is not influenced by the selection of representations for the functions $\{I_i\}_{i=1}^{N_\mathrm{I}}$. In applications of the Vese-Chan level set representation to imaging problems or inverse problems, I_i is typically given by a pixel-based representation,

$$I_i(\mathbf{r};\mathbf{a}_i) = \sum_{k=1}^{N_\mathrm{g}} a_k^i \chi_k(\mathbf{r}), \tag{24}$$

where χ_k is the characteristic function for forward-model grid cell number k. (The elements in $\mathbf{a}$ associated with I_i has been gathered in the vector $\mathbf{a}_i$, such that $\mathbf{a} = \left[\mathbf{a}_1^T, \mathbf{a}_2^T, \ldots, \mathbf{a}_{N_\mathrm{I}}^T\right]^T$.) While this choice results in a very flexible representation for p, it does not lead to a reduced representation for p with respect to a standard pixel-based representation, since the total number of parameters then becomes $(N_\mathrm{c} + N_\mathrm{I} \times N_\mathrm{g})$. To reduce the number of parameters, narrow-band implementations of this algorithm, where only parameters, a_k^i, associated with characteristic functions for grid cells in the vicinity of I_i^0 are allowed to change, has been proposed [32]. This approach requires that one keeps track of the positions on the forward-model grid of all the changing I_i^0's, which can be cumbersome. An alternative way to achieve a reduced representation will be presented in the next section.

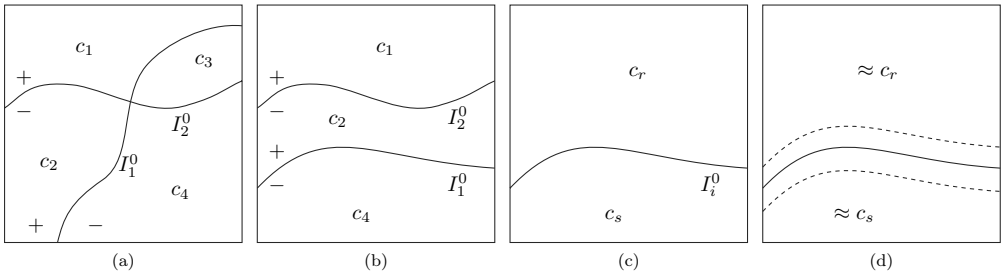

Fig. 1. (a) Zone geometry of level set representation where I_1^0 and I_2^0 intersect. (b) Zone geometry of level set representation where I_1^0 and I_2^0 do not intersect. (c) Detail of level set representation in the vicinity of I_i^0. (d) Detail of smoothed level set representation in the vicinity of I_i^0.

3.1.2. Reduced, smoothed level set representation

Replacing the Heaviside function in (21) by a smoothed approximation [8, 9],

$$\tilde{H}\left(I_i\right) = \frac{1}{\pi}\tan^{-1}\left(I_i\right) + \frac{1}{2}, \tag{25}$$

results in a representation for p that approximates a level set representation, but which is not a zonation since all the corresponding Ψ_j's will have global support. The degree of 'effective overlap' in the support of the different Ψ_j's – and, thereby, the degree to which the representation approximates a level set representation – is controlled by the behavior of the functions, $\{I_i\}_{i=1}^{N_\mathrm{I}}$, in the vicinity of their zero level sets. To illustrate this, let $\mathbf{n}_i(\mathbf{r})$ denote the unit normal vector to I_i^0, and let c_r and c_s denote the values of q in the zones adjacent to I_i^0 that would have resulted from a level set representation of p. Fig. 1c shows a detail of a level set representation for p in the vicinity of (an arbitrary) I_i^0, while Fig. 1d shows the same region when applying the smoothed Heaviside function in (25). The dashed lines indicate the region of effective overlap of the associated basis functions, that is, the region around I_i^0 where $q\left(\mathbf{r};\mathbf{c},\mathbf{a}\right)$ differs significantly from a level set representation. The region of effective overlap – and hence, the smoothness of q – will decrease if $|\nabla I_i \cdot \mathbf{n}_i|$ increase in the vicinity of I_i^0. A numerical study [33] showed that increasing the smoothness of q led to decreasing nonlinearities in the mapping $\mathbf{a} \rightarrow \mathbf{m}$. Although we for this reason would like to aim for relatively smooth representations, q, one must also take into consideration that the earth's subsurface typically has quite sharp transitions between different strata.

To obtain a reduced representation for p, we replace the pixel-based representation for I_i, (24), by a representation where the basis functions are not attached to the forward-model grid [8, 9],

$$I_i\left(\mathbf{r};\mathbf{a}_i\right) = \sum_{k=1}^{N_\mathrm{a}^i} a_k^i \theta_k^i\left(\mathbf{r}\right). \tag{26}$$

Here, $\left\{\theta_k^i\right\}_{k=1}^{N_\mathrm{a}^i}$ denotes a set of basis functions that will be further specified below, and $\mathbf{a}_i = \left[a_1^i, a_2^i, \ldots, a_{N_\mathrm{a}^i}^i\right]^T$ is the associated coefficient vector. To discriminate between the two sets of coefficients, $\mathbf{a} = \left[\mathbf{a}_1^T, \mathbf{a}_2^T, \ldots, \mathbf{a}_{N_\mathrm{I}}^T\right]^T$ and $\mathbf{c} = \left[c_1, c_2, \ldots c_{N_\mathrm{c}}\right]^T$, the former will from now on be denoted interior coefficients while the latter will be denoted exterior coefficients. In line with this, we will from now on denote the functions $\{I_i\}_{i=1}^{N_\mathrm{I}}$ and $\{E_j\}_{j=1}^{N_\mathrm{c}}$, interior functions and exterior functions, respectively. Note that the total number of interior coefficients is $N_\mathrm{a} = \sum_{i=1}^{N_\mathrm{I}} N_\mathrm{a}^i$.

We want the total number of parameters, $(N_\mathrm{c} + N_\mathrm{a})$, to be significantly less than N_g, without loosing the flexibility to model fairly complex subsurface conductivity distributions. To accommodate this, we define a

parameter grid on D consisting of non-overlapping rectangles, where the area of a typical rectangle is much larger than that of a typical forward-model grid cell. (A 3×3 parameter grid is illustrated in Fig. A.19a in Appendix A.) Since the interior functions will be represented on this grid in a finite-element fashion, the cells are denoted parameter elements and the cell corners are denoted parameter nodes. The function θ_k^i has support on parameter elements adjacent to parameter node no. k. On each of these elements, θ_k^i is represented by a bilinear function with support on that element. The four normalized bilinear functions associated with an arbitrary parameter element defined by $[x_1, x_2] \times [z_1, z_2]$ are

$$\left((x_2 - x_1)(z_2 - z_1)\right)^{-1} \begin{cases} (x_2 - x)(z_2 - z) \\ (x - x_1)(z_2 - z) \\ (x - x_1)(z - z_1) \\ (x_2 - x)(z - z_1) \end{cases} . \tag{27}$$

This type of parameter function representation was introduced in [8] and extended to 3D in [9]. Both these papers were concerned with the case of $N_{\mathrm{I}} = 1$, and hence, $N_{\mathrm{c}} = 2$. In [8], it was shown that reducing N_{a} led to reduced nonlinearities in the mapping $\mathbf{a} \to \mathbf{m}$.

In this paper, we extend the parameter representation to $N_{\mathrm{I}} > 1$, to be able to model more than two large-scale subsurface structures with different electric conductivity. Although it is possible to define different parameter grids for each interior function, we will in this paper apply a single parameter grid, hence $N_{\mathrm{a}}^i = N; i = 1, 2, \ldots, N_{\mathrm{I}}$, and $N_{\mathrm{a}} = N_{\mathrm{I}} \times N$. Furthermore, we assume that the exterior coefficients are independent of $\mathbf{r}$ and known a priori, and focus on the challenging problem of identification of multiple large-scale structures with weak conductivity contrasts. (See, however, Section 6 for a brief discussion of the case when the exterior coefficients are unknown as well.) Two simple examples, showing in detail how the parameterization works, are found in Appendix A.

It can be difficult to choose the dimensionality of the reduced representation such that it corresponds well with the information content implicitly given by the data. A well-known strategy is to start with a coarse representation and gradually refine it during the estimation. An adaptive multilevel estimation strategy, introduced in [34] for standard zonation, was extended to non-standard zonation in [9], where the number of interior coefficients was increased locally in regions inferred automatically from the available data. In this work, however, we keep the number of interior coefficients fixed during the estimation under the assumption that the required spatial variability of the interior functions is approximately known from the structures underlying the prior model.

3.2. Shape priors

To build the prior PDF, we assume that a set of uncertain subsurface structures, potentially interpreted from seismic data, is available to us. We gather these structures in a *training data* set; a term taken from machine learning. The training data should reflect the type of interpreted structures, and also the uncertainty in the interpretation. We want to construct a prior PDF based on the distribution of structures, or more precisely, the distribution of interior coefficients in the training data set. As discussed in the introduction, a multivariate gaussian prior PDF may not be appropriate for our application. In addition to the arguments presented there, a prior PDF built from two or more training data sets will necessarily be multimodal, and therefore non-gaussian.

The limitation of assuming a gaussian prior distribution in parameter space was also observed in [18], for an image segmentation problem. They proposed a solution where non-gaussian behavior can be incorporated in the prior PDF. We will now summarize the proposed method, and also argue for some adjustments made to adapt the method to the inverse problem under consideration.

3.2.1. Shape prior regularization term

Let $\left\{\mathbf{t}^i\right\}_{i=1}^m \in \mathbb{R}^{N_{\mathrm{a}}}$ be a set of training data. Each $\mathbf{t}^i$ consists of a unique set of values for the interior coefficients associated with all the interior functions involved in representing a subsurface model, $\mathbf{t}^i = \mathbf{a}^i$.

Further, let ϕ be a nonlinear transformation from the parameter space $\mathbb{R}^{N_a}$ to a *feature space* $\mathcal{Y}$

$$\phi : \mathbb{R}^{N_a} \to \mathcal{Y}.$$

We remark that $\mathcal{Y}$ could be arbitrarily large, or possibly infinite dimensional. The sample mean and covariance of the training data in $\mathcal{Y}$ is

$$\phi_0 = \frac{1}{m}\sum_{i=1}^{m} \phi\left(\mathbf{t}^i\right), \tag{28}$$

$$\tilde{\mathbf{\Sigma}} = \frac{1}{m}\sum_{i=1}^{m} \left(\phi\left(\mathbf{t}^i\right) - \phi_0\right)\left(\phi\left(\mathbf{t}^i\right) - \phi_0\right)^T. \tag{29}$$

Denoting $\tilde{\phi}\left(\mathbf{a}\right) = \phi\left(\mathbf{a}\right) - \phi_0$, the regularization term J_{prior} is defined as

$$J_{\text{prior}}\left(\mathbf{a}\right) = \tilde{\phi}\left(\mathbf{a}\right)^T \mathbf{\Sigma}^{-1} \tilde{\phi}\left(\mathbf{a}\right). \tag{30}$$

Note that $\mathbf{\Sigma}$ is a regularized covariance matrix given as [18]

$$\begin{aligned} \mathbf{\Sigma} &= \tilde{\mathbf{\Sigma}} + \lambda_\perp \left(\mathbf{I} - \mathbf{V}\mathbf{V}^T\right) \\ &= \mathbf{V}\mathbf{\Lambda}\mathbf{V}^T + \lambda_\perp \left(\mathbf{I} - \mathbf{V}\mathbf{V}^T\right), \end{aligned} \tag{31}$$

where $\mathbf{\Lambda} = \text{diag}\left(\lambda_k\right)$ – with $\{\lambda_k\}_{k=1}^r$ being the $r \leq m$ positive eigenvalues of $\tilde{\mathbf{\Sigma}}$ in descending order, and where $\mathbf{V} = \left[\mathbf{v}^1, \mathbf{v}^2, \ldots, \mathbf{v}^r\right]$ – with $\mathbf{v}^k$ being the normalized eigenvector corresponding to λ_k. The positive constant $\lambda_\perp$ replaces potential zero eigenvalues of $\tilde{\mathbf{\Sigma}}$, and is in our case selected as $\lambda_\perp = \lambda_r/2$ [18]. The reason for using $\mathbf{\Sigma}$ in (30) instead of $\tilde{\mathbf{\Sigma}}$, is that $\tilde{\mathbf{\Sigma}}$ is estimated from the mapped training data, $\left\{\tilde{\phi}\left(\mathbf{t}^i\right)\right\}_{i=1}^m$, which only spans a subspace, $\mathcal{F}$, of $\mathcal{Y}$. Since J_{prior} is a type of Mahalanobis distance measure for the whole space $\mathcal{Y}$, the covariance matrix $\tilde{\mathbf{\Sigma}}$ will not be a correct weighting criterion for this measure. Informally speaking, the last term in (31) open for the possibility of solutions which are not in the span of the training data, but since $\lambda_\perp < \lambda_r$ they are less probable than all solutions within the span of the training data.

The regularization term, J_{prior}, as defined in (30), is the corresponding energy of a gaussian probability density in $\mathcal{Y}$. Hence, the training data are transformed from $\mathbb{R}^{N_a}$, where they are not normally distributed, to $\mathcal{Y}$, where they by construction are normally distributed. The disadvantage, at the outset, is that we do not know the nonlinear map ϕ or the feature space $\mathcal{Y}$. However, as it turns out, explicit information about ϕ and $\mathcal{Y}$ is not needed when calculating J_{prior}.

The expression in (30), as it stands, cannot be calculated directly. To further develop the expression, we insert (31) into (30) to get

$$\begin{aligned} J_{\text{prior}}\left(\mathbf{a}\right) &= \tilde{\phi}\left(\mathbf{a}\right)^T \mathbf{\Sigma}^{-1} \tilde{\phi}\left(\mathbf{a}\right), \\ &= \tilde{\phi}\left(\mathbf{a}\right)^T \left(\mathbf{V}\mathbf{\Lambda}\mathbf{V}^T + \lambda_\perp \left(\mathbf{I} - \mathbf{V}\mathbf{V}^T\right)\right)^{-1} \tilde{\phi}\left(\mathbf{a}\right), \\ &= \tilde{\phi}\left(\mathbf{a}\right)^T \left(\mathbf{V}\mathbf{\Lambda}^{-1}\mathbf{V}^T + \lambda_\perp^{-1} \left(\mathbf{I} - \mathbf{V}\mathbf{V}^T\right)\right) \tilde{\phi}\left(\mathbf{a}\right). \end{aligned} \tag{32}$$

Written as a series expansion (32) reads

$$J_{\text{prior}}\left(\mathbf{a}\right) = \sum_{k=1}^{r} \lambda_k^{-1} \left\langle \mathbf{v}^k, \tilde{\phi}\left(\mathbf{a}\right)\right\rangle^2 + \lambda_\perp^{-1} \left(\left\langle \tilde{\phi}\left(\mathbf{a}\right), \tilde{\phi}\left(\mathbf{a}\right)\right\rangle - \sum_{k=1}^{r} \left\langle \mathbf{v}^k, \tilde{\phi}\left(\mathbf{a}\right)\right\rangle^2\right). \tag{33}$$

In (33) we have, in addition to $\tilde{\phi}\left(\mathbf{a}\right)$, the quantities λ_k and $\mathbf{v}^k$ that are unknown. To determine these quantities, we first note that by the definition of $\tilde{\mathbf{\Sigma}}$, its eigenvectors, $\mathbf{v}^k$, can be expressed as a series expansion of the mapped training data

$$\mathbf{v}^k = \sum_{i=1}^{m} \alpha_i^k \tilde{\phi}\left(\mathbf{t}^i\right), \qquad k = 1, \ldots, r, \tag{34}$$

thus reducing the search for $\mathbf{v}^k$ to finding the expansion coefficients $\{\alpha_i^k\}_{i=1}^m$.

To acquire λ_k and $\{\alpha_i^k\}_{i=1}^m$, we use the kernel principal component analysis (kPCA) method established by Schölkopf *et al* in [35]. They showed that λ_k and $\{\alpha_i^k\}_{i=1}^m$ can be found in terms of the eigenvalues and eigenvectors of a centered kernel matrix. The centered kernel matrix is a $m \times m$ Gram matrix, $\tilde{\mathbf{K}}$, where $\tilde{\mathbf{K}}_{ij} = \tilde{k}\left(\mathbf{t}^i, \mathbf{t}^j\right)$. The function $\tilde{k}$ is called the centered kernel function and is defined as

$$\tilde{k}\left(\mathbf{u}, \mathbf{w}\right) = \left\langle \tilde{\phi}\left(\mathbf{u}\right), \tilde{\phi}\left(\mathbf{w}\right) \right\rangle, \tag{35}$$

where $\mathbf{u}, \mathbf{w} \in \mathbb{R}^{N_\mathrm{a}}$. From kPCA, the eigenvalues of $\tilde{\mathbf{K}}$, $\tilde{\lambda}_k$, are linked with λ_k through the relation

$$\lambda_k = \frac{\tilde{\lambda}_k}{m},$$

and the eigenvectors of $\tilde{\mathbf{K}}$ are the expansion coefficients $\boldsymbol{\alpha}^k = \left[\alpha_1^k, \ldots, \alpha_m^k\right]^T$ in (34), normalized with $1/\sqrt{\tilde{\lambda}_k}$.

We finalize the derivation of J_prior by inserting (34) into (33), which yields

$$\begin{aligned} J_\mathrm{prior}\left(\mathbf{a}\right) &= \sum_{k=1}^{r} \lambda_k^{-1} \left(\sum_{i=1}^{m} \alpha_i^k \left\langle \tilde{\phi}\left(\mathbf{t}^i\right), \tilde{\phi}\left(\mathbf{a}\right) \right\rangle \right)^2 + \lambda_\perp^{-1} \left(\left\langle \tilde{\phi}\left(\mathbf{a}\right), \tilde{\phi}\left(\mathbf{a}\right) \right\rangle \right. \\ &\quad \left. - \sum_{k=1}^{r} \left(\sum_{i=1}^{m} \alpha_i^k \left\langle \tilde{\phi}\left(\mathbf{t}^i\right), \tilde{\phi}\left(\mathbf{a}\right) \right\rangle \right)^2 \right), \\ &= \sum_{k=1}^{r} \left(\sum_{i=1}^{m} \alpha_i^k \tilde{k}\left(\mathbf{t}^i, \mathbf{a}\right) \right)^2 \left(\lambda_k^{-1} - \lambda_\perp^{-1}\right) + \lambda_\perp^{-1} \tilde{k}\left(\mathbf{a}, \mathbf{a}\right), \end{aligned} \tag{36}$$

when using (35) to obtain the last equality. Comparing (36) and (30) it is clear that the problem of calculating J_prior has been reduced to finding a suitable centered kernel function $\tilde{k}$.

In general, relations on the form of (35) are called *the kernel trick*. It enables transformation of data points from the input space $\mathbb{R}^{N_\mathrm{a}}$ to some (possibly) higher dimensional space $\mathcal{Y}$, where inner products are used to extract features in the data which are not available in $\mathbb{R}^{N_\mathrm{a}}$. This has been exploited in many branches of science, for example machine learning (see, e.g., [36–39]) and reservoir geostatistics (see, e.g., [40, 41]).

The centered kernel function is, however, evaluated via an uncentered kernel function, k, which needs to be selected by the user according to the problem at hand. (From now on, we will drop the term 'uncentered' when discussing such functions.) In the next sections, we discuss proper selection of k within two function classes, and elaborate on our specific choice for the application considered.

3.2.2. Properties of positive definite and conditionally positive definite kernels

We consider the class of (symmetric and real-valued) conditionally positive definite (CPD) kernel functions, and its sub class; positive definite (PD) kernel functions. Let $\mathbf{K}$ be the Gram matrix associated with the kernel function k, that is $K_{ij} = k\left(\mathbf{t}^i, \mathbf{t}^j\right)$, and let $\mathbf{1}$ denote the m-vector where each element equals 1. A kernel function is said to be PD iff $\mathbf{s}^T\mathbf{K}\mathbf{s} \geq 0 \quad \forall \mathbf{s}$, and CPD if $\mathbf{s}^T\mathbf{K}\mathbf{s} \geq 0 \quad \forall \mathbf{s} | \mathbf{s}^T\mathbf{1} = 0$.

Two relations will be useful for discussing the properties of PD and CPD kernels. Firstly, the following relation must hold between $\tilde{k}$ and any CPD k in order for the latter to be a valid choice [39]

$$\tilde{k}\left(\mathbf{u}, \mathbf{w}\right) = k\left(\mathbf{u}, \mathbf{w}\right) - \sum_{i=1}^{m} \psi_i k\left(\mathbf{u}, \mathbf{t}^i\right) - \sum_{i=1}^{m} \psi_i k\left(\mathbf{w}, \mathbf{t}^i\right) + \sum_{i,j=1}^{m} \psi_i \psi_j k\left(\mathbf{t}^i, \mathbf{t}^j\right), \tag{37}$$

where $\sum_{i=1}^m \psi_i = 1$. The specific choice $\psi_i = 1/m$ leads to

$$\tilde{k}\left(\mathbf{u}, \mathbf{w}\right) = k\left(\mathbf{u}, \mathbf{w}\right) - \frac{1}{m} \sum_{i=1}^{m} \left[k\left(\mathbf{u}, \mathbf{t}^i\right) + k\left(\mathbf{w}, \mathbf{t}^i\right)\right] + \frac{1}{m^2} \sum_{i,j=1}^{m} k\left(\mathbf{t}^i, \mathbf{t}^j\right). \tag{38}$$

Common choices of kernels fulfill (38), and we consider only such kernels in this paper. Secondly, any valid PD and CPD kernels must obey the following relation [42]

$$k_{PD}(\mathbf{u},\mathbf{w}) = \nu\left[k_{CPD}(\mathbf{u},\mathbf{w}) - k_{CPD}(\mathbf{u},\mathbf{u}_0) - k_{CPD}(\mathbf{u}_0,\mathbf{w}) + k_{CPD}(\mathbf{u}_0,\mathbf{u}_0)\right], \tag{39}$$

where $\mathbf{u}_0$ and ν are arbitrary.

PD kernels. According to *Mercer's theorem* [43] there exists a PD k such that $k(\mathbf{u},\mathbf{w}) = \langle\phi(\mathbf{u}),\phi(\mathbf{w})\rangle$. Thus, $\mathcal{Y}$ is a Hilbert space with inner product $k(\mathbf{u},\mathbf{w})$.

PD kernels allows for an easy derivation of (38). Inserting $\tilde{\phi}(\mathbf{a}) = \phi(\mathbf{a}) - \phi_0$ into (35), and recalling the definition of ϕ_0 from (28), yields

$$\begin{aligned}\tilde{k}(\mathbf{u},\mathbf{w}) &= \left\langle \phi(\mathbf{u}) - \frac{1}{m}\sum_{i=1}^{m}\phi\left(\mathbf{t}^i\right), \phi(\mathbf{w}) - \frac{1}{m}\sum_{j=1}^{m}\phi\left(\mathbf{t}^j\right)\right\rangle \\ &= \langle\phi(\mathbf{u}),\phi(\mathbf{w})\rangle - \frac{1}{m}\sum_{i=1}^{m}\left\langle\phi(\mathbf{w}),\phi\left(\mathbf{t}^i\right)\right\rangle - \frac{1}{m}\sum_{j=1}^{m}\left\langle\phi(\mathbf{u}),\phi\left(\mathbf{t}^j\right)\right\rangle \\ &\quad + \frac{1}{m^2}\sum_{i,j=1}^{m}\left\langle\phi\left(\mathbf{t}^i\right),\phi\left(\mathbf{t}^j\right)\right\rangle.\end{aligned} \tag{40}$$

Inserting $\langle\phi(\mathbf{u}),\phi(\mathbf{w})\rangle = k(\mathbf{u},\mathbf{w})$ into (40) yields (38).

CPD kernels. The squared distance in $\mathcal{Y}$ can be expressed

$$\begin{aligned}\|\phi(\mathbf{u}) - \phi(\mathbf{w})\|^2 &= \langle\phi(\mathbf{u}),\phi(\mathbf{u})\rangle - 2\langle\phi(\mathbf{u}),\phi(\mathbf{w})\rangle + \langle\phi(\mathbf{w}),\phi(\mathbf{w})\rangle \\ &= k_{PD}(\mathbf{u},\mathbf{u}) - 2k_{PD}(\mathbf{u},\mathbf{w}) + k_{PD}(\mathbf{w},\mathbf{w}),\end{aligned} \tag{41}$$

where Mercer's theorem has been applied to obtain the last equality. Inserting (39) into (41) leads to

$$k(\mathbf{u},\mathbf{w}) = \frac{1}{2}\left[k(\mathbf{u},\mathbf{u}) + k(\mathbf{w},\mathbf{w})\right] - \|\phi(\mathbf{u}) - \phi(\mathbf{w})\|^2. \tag{42}$$

where ν has been set equal to $1/2$ for convenience. Thus, $\mathcal{Y}$ is a Hilbert space where (42) gives the relation between its distance measure and $k(\mathbf{u},\mathbf{w})$ [42].

3.2.3. Selection of kernel

The gaussian kernel

$$k(\mathbf{u},\mathbf{w}) = \frac{1}{\left(2\pi h^2\right)^{\frac{N_\mathrm{a}}{2}}}\exp\left(-\frac{\|\mathbf{u}-\mathbf{w}\|^2}{2h^2}\right), \tag{43}$$

which is PD, has been the most popular choice, see, for example, [18]. The following toy example will, however, illustrate why we do not think the gaussian kernel is appropriate for our application.

Fig. 2a shows three clusters (red dots) of training data, $\mathbf{t}^i \in \mathbb{R}^2$. Using the gaussian kernel function with these training data, the contour plot of J_prior in Fig. 2b is obtained. It is seen that J_prior has an approximately constant magnitude, except in the immediate vicinity of the training data. This is a rather unfortunate feature of the gaussian kernel when applied in conjunction with a gradient based optimization methodology. It suggest that if the current estimate is far away from the training data set, virtually no influence from J_prior will occur. Assuming that the prior model does not contain misleading information, it is precisely at such locations of the current estimate that helpful contributions from the prior model is most needed, to avoid that the optimization method stops at a non-global minimum of J_data.

As an alternative to the gaussian kernel, we consider a particular CPD kernel – the power kernel

$$k(\mathbf{u},\mathbf{w}) = \frac{1}{h^{N_\mathrm{a}}}\begin{cases}\rho(\tau,N_\mathrm{a}) - \left\|\frac{\mathbf{u}-\mathbf{w}}{h}\right\|^\tau, & \text{if } \left\|\frac{\mathbf{u}-\mathbf{w}}{h}\right\| \le \rho(\tau,N_\mathrm{a})^{\frac{1}{\tau}}, \\ 0, & \text{otherwise,}\end{cases} \tag{44}$$

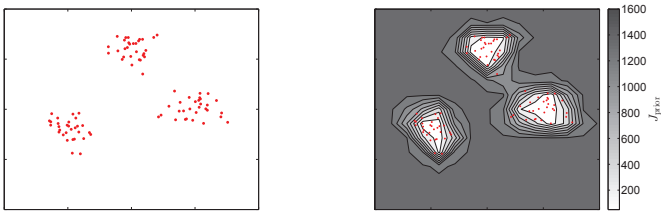

(a) (b)

Fig. 2. Example of J_{prior} with gaussian kernel: (a) training data set, (b) training data set and contours of J_{prior}. The hyperparameter h in (43) is chosen according to [18].

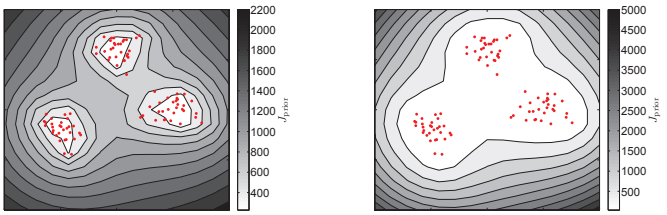

(a) (b)

Fig. 3. Training data set and contours of J_{prior} with the power kernel with two values for τ inserted in (44): (a) $\tau = 0.5$, (b) $\tau = 1.5$. The hyperparameter h in (44) is chosen such that $k \neq 0$

where $0 \leq \tau \leq 2$ and

$$\rho\left(\tau, N_{\text{a}}\right) = \left(\frac{\tau + N_{\text{a}}}{\tau V_{N_{\text{a}}}}\right)^{\frac{\tau}{\tau + N_{\text{a}}}},$$

with $V_{N_{\text{a}}}$ being the volume of the unit N_{a}-dimensional sphere ($V_1 = 2$, $V_2 = \pi$, $V_3 = 4\pi/3$, etc). Contour plots of J_{prior} when applying the power kernel with two values of τ are shown in Fig. 3. It is seen that the three clusters are encapsulated in similar fashion as with the gaussian kernel, but more importantly for our application, J_{prior} is convexly shaped outside the perimeter of the training data. Thus, use of the power kernel ensures a positive contribution from the prior term in the optimization at locations where it is most needed.

In [44, Appendix C], and [18], it was argued for use of PD kernels, since this led to an interpretation of J_{prior} as a generalization of the Parzen kernel density estimator [45] for multivariate data. It is, however, possible to follow exactly the same line of arguments also for CPD kernels, since the key point is use of (38).

In summary, we choose the power kernel function (44) as it, from the above discussion, was shown to have a computational advantage in our application, and moreover, it did not lead to any loss of theoretical properties for J_{prior}.

4. Optimization

For the minimization of the objective function, (17), the Levenberg-Marquardt (LM) algorithm, as given by Fletcher [46], is applied. (The parameterization and shape prior methodologies presented in this paper

could, of course, have been combined with alternative optimization algorithms as well.) At iteration step k, the LM linear system for a step $\Delta\mathbf{a}^k$ can be written as follows

$$\left[\mathbf{H}\left(\mathbf{a}^k\right) + \eta^k \mathbf{I}\right] \Delta\mathbf{a}^k = -\nabla O\left(\mathbf{a}^k\right), \tag{45}$$

where the gradient of the objective function is given by

$$\nabla O\left(\mathbf{a}^k\right) = 2\mathbf{S}\left(\mathbf{a}^k\right)^T \mathbf{C}^{-1}\left(\mathbf{m}\left(\mathbf{a}^k\right) - \mathbf{d}\right) + \beta^k \nabla J_{\text{prior}}\left(\mathbf{a}^k\right), \tag{46}$$

and the Hessian of (17) is given by

$$\mathbf{H}\left(\mathbf{a}^k\right) = 2\mathbf{S}\left(\mathbf{a}^k\right)^T \mathbf{C}^{-1}\mathbf{S}\left(\mathbf{a}^k\right) + \beta^k \nabla\left(\left(\nabla J_{\text{prior}}\left(\mathbf{a}^k\right)\right)^T\right). \tag{47}$$

$\mathbf{S}(\mathbf{a})$ is the sensitivity matrix $\mathrm{d}\mathbf{m}/\mathrm{d}\mathbf{a}$, which is found using the direct (or gradient simulator) method, see, e.g., [47]. The computational cost in finding $\mathbf{S}$ is reduced due to the stiffness matrix $\mathbf{A}$ being common both in solving the forward problem and calculating the sensitivity; see Appendix B. The derivatives of the shape prior term can be calculated analytically, and is described in Appendix C.

The model update, (45), is computationally highly intensive for a large number of parameters, due to computation of $\mathbf{H}$. With a pixel-based representation, use of LM is therefore restricted to smaller problems. The reduced representation of the parameter function employed here, however, allows for larger models in terms of the number of forward-model grid cells.

When a satisfactory step has been found according to the implementation of LM given in [46], the interior coefficients are updated as follows

$$\mathbf{a}^{k+1} = \mathbf{a}^k + \Delta\mathbf{a}^k.$$

Following [48], the optimization is terminated if the following three criteria are satisfied: (i) the difference between the objective function value, O, in two successful steps is smaller than a predetermined tolerance; (ii) the length of a successful step, $\|\Delta\mathbf{a}\|$, is smaller than a predetermined tolerance; (iii) the norm of the gradient of the objective function, $\|\nabla O\|$, is smaller than a predetermined value. The optimization is also terminated if the number of iterations or η^k attains a predetermined maximum value.

In the literature, there has been several suggestions concerning the choice of regularization parameter β and how it should be varied during the optimization (see, e.g., [49]). The general consensus is that the parameter should be large in the beginning of the optimization to reflect the confidence we have in the prior model, and be decreased during the optimization such that the final iterations are mainly driven by J_{data}. In the optimization, β is decreased by a predetermined factor in each successful iteration, i.e., $\beta^{k+1} = \gamma\beta^k$, where $0 < \gamma < 1$.

Though beyond the scope of this paper, we mention that in the literature different approaches are presented to improve the vertical resolution in the interpretation of CSEM data, e.g., by combining multiple frequencies (see, e.g., [50]) and the use of model weighting schemes (see, e.g., [13, 51]).

5. Numerical experiments

In this section, we apply our model-based inversion methodology on various synthetic CSEM test cases. In all the test cases, we have a 2D cross-section as shown in Fig. 4a. The geoelectric model consists of a resistive air layer with conductivity 10^{-6} S/m from $z = -20$ to $z = 0$ km. The sea layer, with conductivity 3.33 S/m, is between $z = 0$ to $z = 1.5$ km, and we assume flat bathymetry (i.e. flat sea-floor). In the subsurface we have the inversion domain $D = \{\mathbf{r} \mid x \in [-6.5, 6.5], z \in [1.5, 3.5]\}$ km^2 (c.f. Fig. 4a), where we in the test cases have different large-scale geological structures which we seek to identify. The union of geological structures will be referred to as a subsurface model, or alternatively, a model. We let D be large in the lateral and vertical direction such that influence from the surrounding subsurface areas can be neglected. The surrounding subsurface areas are given fixed conductivity value of 1 S/m.

For the numerical CSEM survey, we used a horizontal electric dipole source towed 50 m above the sea-floor emitting signals with frequency 0.25 Hz. We used 8 source positions evenly distributed in $\{(x, y) \mid$

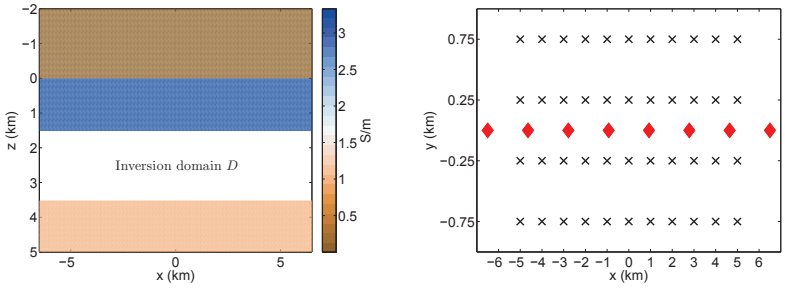

(a) (b)

Fig. 4. Experimental setup: (a) vertical cross-section with inversion domain, (b) horizontal positions of sea floor receivers (black crosses) and source (red diamonds).

$x \in [-6.5, 6.5], y = 0\}$ km. We utilized a total of 44 sea-floor receivers which were evenly distributed in a 2D array with 500 m interval in the y-direction and 1 km interval in the x-direction, covering the area $R = \{(x, y) \mid x \in [-5, 5], y \in [-0.75, 0.75]\}\,\mathrm{km}^2$ (confer Fig. 4b).

To generate synthetic observed data, $\mathbf{d}$, we added 5% gaussian noise to the forward model output, $\mathbf{e} = [e_x, e_y, e_z]^T$, obtained with the reference conductivity distribution. Data points from receivers less than 1.5 km away from the source position were removed to avoid influence from the direct wave (i.e. signals propagating directly from source to receivers).

For each test case, the reference subsurface model is constructed using the parameter representation given in section 3.1. Hence, the transition between each conductivity region is continuous, but chosen to be relatively sharp. The initial subsurface models are generated with the same transition sharpness as the reference models.

In the inversion process, we let $N = 9$, and $N_\mathrm{I} \leq 3$. The maximum number of interior coefficients used in the test cases is then 27, while the number of grid cells in D is approximately 16 000. Thus, $N_\mathrm{a} \ll N_\mathrm{g}$ in all the test cases, facilitating use of the LM optimization algorithm.

When shape prior regularization is applied, the shape prior is constructed from one or two training data sets. A training data set consists of 20 sample vectors, $\left\{\mathbf{t}^i\right\}_{i=1}^{20}$, where each element in $\mathbf{t}^i$ is drawn from a uniform distribution centered around a predetermined mean value.

When a single training data set is employed, we mimic a situation where seismic interpretation has resulted in a consensus about the type of geological structural model, but where the exact shape and placement of the structures are uncertain. When two training data sets are employed, we mimic a situation where the seismic interpretation has resulted in two equally probable types of geological models, with intrinsic uncertainty in each model type. The reference solution is not a member of the training data set in any of the test cases.

To demonstrate the performance of our inversion methodology, we do two inversions per test case: first inverting observed data alone, and second, inverting observed data with shape prior regularization. This way we show how the reduced representation perform by itself, and subsequently what the impact of applying the shape prior technique is. When we apply shape prior regularization, we use the power kernel given in (44) with $\tau = 1.5$ and h such that $k \neq 0$ unless otherwise stated. Furthermore, the regularization parameter, β, is chosen such that J_data and J_prior is equal initially and is then reduced by a factor $\gamma = 0.9$ unless otherwise stated.

5.1. Test case 1: Anticline model

In this test case we consider an anticline model shown in Fig. 5a. The reference solution was made using 2 interior functions to represent 3 layers with different conductivity values. The conductivity values of the

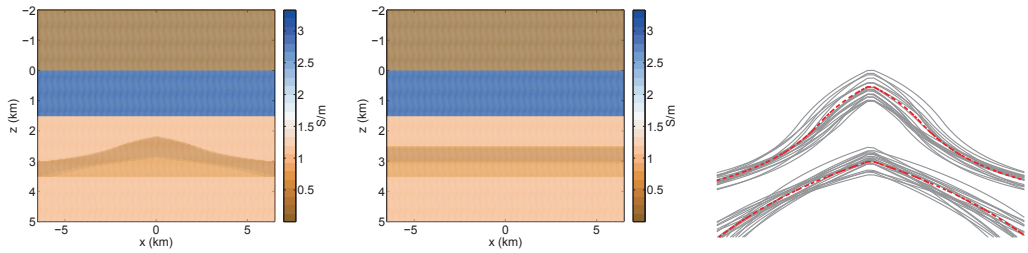

Fig. 5. Test case 1: (a) reference model, (b) initial model, (c) training data set (grey), and I_1^0 and I_2^0 for the reference model (dashed red).

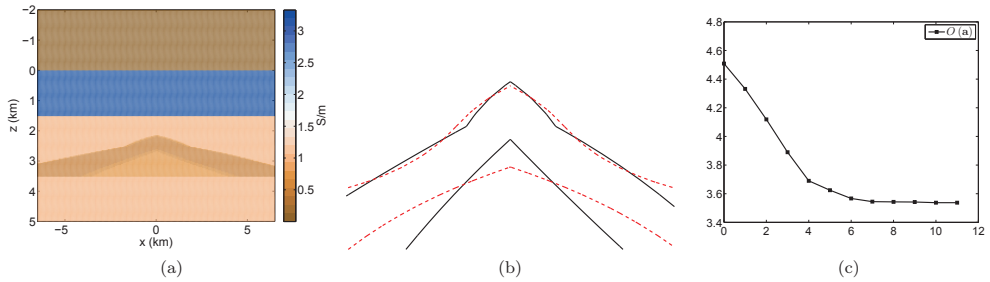

Fig. 6. Inversion result of test case 1 using only observed data: (a) final model, (b) I_1^0 and I_2^0 of final model (solid black) and reference model (dashed red), (c) log-objective function value versus iteration count.

different layers are from top to bottom: 1 S/m, 0.5 S/m and 0.67 S/m. Note the low conductivity contrast between the layers; at most of ratio 1:2.

Inversion of observed data

In Fig. 5b and 6a, we see the initial and final models of the inversion, respectively. The initial model consists of horizontal layers, that is, there is no indication of any anticline structure. The final model has the appearance of an anticline type model, but does not recreate the reference model exactly. This is seen more clearly in Fig. 6b where we compare the zero levels of the interior functions from the final model (solid black) and reference model (dashed red). The shape of the upper boundary is fairly close to the upper boundary of the reference model, whereas the bottom boundary describes a triangle shape not matching the curved shape in the reference model. This suggests that there was enough sensitivity in the data to approximately identify the upper boundary of the anticline model, but the limited vertical resolution made it difficult to identify the bottom boundary.

Inversion of observed data with shape prior

To build the shape prior PDF we used the training data illustrated in Fig. 5c. Although the mean of the prior PDF would constitute a natural initial model, we apply the same initial model as when no prior model was used. If we had applied the mean of the prior PDF as initial model, the initial model would have been much closer to the reference model.

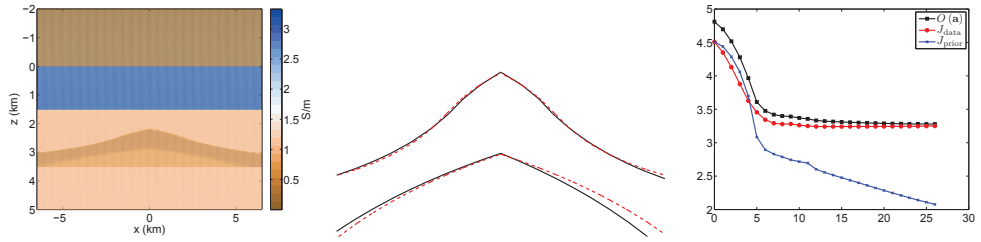

(a) (b) (c)

Fig. 7. Inversion result of test case 1 using observed data with shape prior regularization: (a) final model, (b) I_1^0 and I_2^0 of final model (solid black) and reference model (dashed red), (c) log-objective function values versus iteration count.

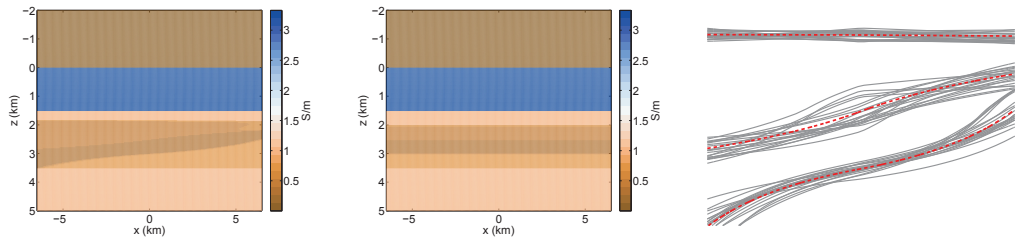

(a) (b) (c)

Fig. 8. Test case 2: (a) reference model, (b) initial model, (c) training data set (grey), and I_1^0, I_2^0 and I_3^0 for the reference model (dashed red).

The final result of the inversion of observed data with shape prior regularization is shown in Fig. 7a. The final model shows good correspondence with the reference model as further emphasized in Fig. 7b. The upper boundary is identified almost exactly while the bottom layer is identified with good accuracy.

From comparing the final result with and without shape prior regularization in this test case we see the benefit of introducing prior knowledge, especially for identifying the bottom boundary.

5.2. Test case 2: Four-layer model

We expand the number of layers to four, and consider the model given in Fig. 8a. The reference model consists of a horizontal layer at the top, and below this we have 3 layers where the middle one represents a dipping strata. The model was made using 3 interior functions to separate the 4 conductivity regions. Starting from the top layer the conductivity in each layer is as follows: 1 S/m, 0.5 S/m, 0.33 S/m and 0.67 S/m. Again we have in the subsurface a low conductivity contrast between the layers; at most of ratio 1:3.

Inversion of observed data

The initial model (Fig. 8b) consists of horizontal layers, that is, there is no indication of any dipping structure. From Fig. 8b and 9a, it is seen that only minor changes in the subsurface model have taken place during the inversion, hence the final model does not approximate the reference model well; see Fig. 9b. From Fig. 9c it is seen that these minor changes correspond to a reduction of the objective function by approximately an order of magnitude.

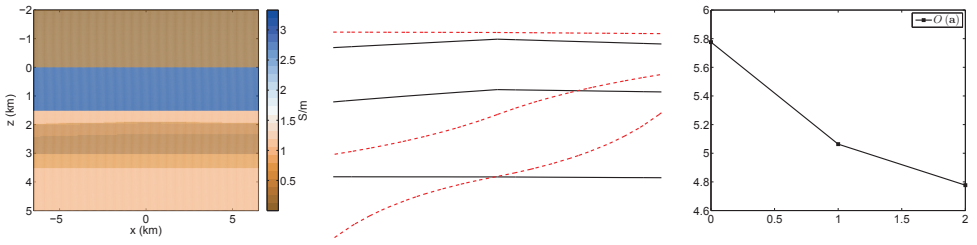

(a) (b) (c)

Fig. 9. Inversion result of test case 2 using only observed data: (a) final model, (b) I_1^0, I_2^0 and I_3^0 of final model (solid black) and reference model (dashed red), (c) log-objective function value versus iteration count.

The optimization was terminated due to η^k exceeding a predetermined maximum value, which suggest that no suitable step, $\Delta \mathbf{a}^k$, was found during the LM optimization. Several attempts with different initial η^0 were made without improving the result. Several different initial models with increasing distance from the reference model in terms of the objective function value were also tested. The same result as above was observed: the resulting models were close to the initial models. Hence the initial model needed to be very close to the reference model to obtain an accurate estimate.

Inversion of observed data with shape prior

The set of training data used in the prior model is illustrated in Fig. 8c. We apply the same initial model as when no prior model was used. To overcome the difficulty of updating the initial model seen in the inversion of observed data alone, we let J_{prior} be twice the value of J_{data} initially.

The final model is shown in Fig. 10a. It approximates the reference model quite well, but some deviations can be seen, especially in the bottom boundary; see Fig. 10b. Nevertheless, it is clear that shape prior regularization was crucial to obtain a good estimate for this problem.

From Fig. 10c, it is seen that J_{data} attains its minimum at iteration 7, while O decreases steadily as the iteration progress. This also highlights the challenge of optimally adjusting β when including a shape prior regularization term in the objective function. Better results could possibly have been made with an improved reduction scheme on β. On the other hand, tuning β with the nonlinear shape prior regularization term is not a trivial task (see, e.g., [23]); for this reason we chose the ad hoc method of reducing β by a predetermined factor γ.

5.3. Test case 3: Four-layer model with two training data sets

We consider the four-layer reference model introduced in test case 2, but test the inversion methodology in a different manner. We add a second training data set – consisting of pinchout structures – (Fig. 11a) to the training data set used in test case 2. The prior model is thus built from two different training data sets. This corresponds to a situation where the geologist(s) interpreting the seismic data have come up with two equally probable structure types. The objective is to investigate into the inversion methodology's ability to identify the reference solution when the prior PDF is bimodal, and where one of the modes corresponds well with the reference model while the other does not. To do an unbiased assessment, we select the initial model as the mean of the training data (i.e. we take the mean of all the interior coefficients in the two training data sets).

Inversion of observed data

The initial and final models are shown in Fig. 11b and 12a, respectively. The final model has only changed from the initial model in the upper half of the inversion domain. From Fig. 12c, we see that the

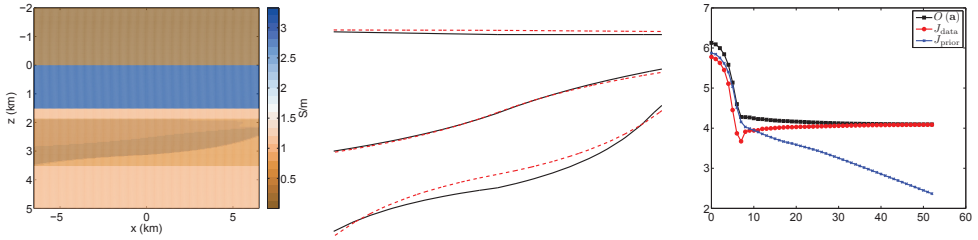

(a) (b) (c)

Fig. 10. Inversion result of test case 2 using observed data with shape prior regularization: (a) final model, (b) I_1^0, I_2^0 and I_3^0 of final model (solid black) and reference model (dashed red), (c) log-objective function values versus iteration count.

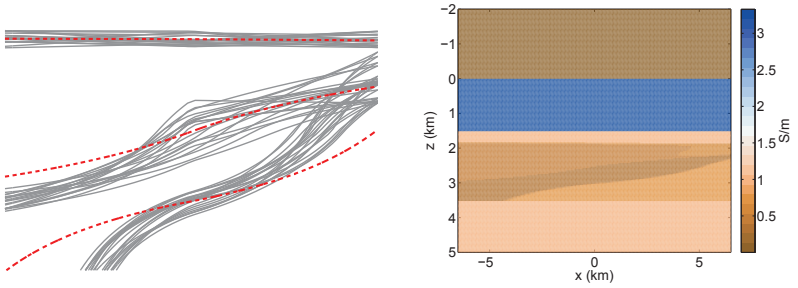

(a) (b)

Fig. 11. Test case 3: (a) pinchout training data set (grey), and I_1^0, I_2^0 and I_3^0 for the reference model (dashed red), (b) initial model.

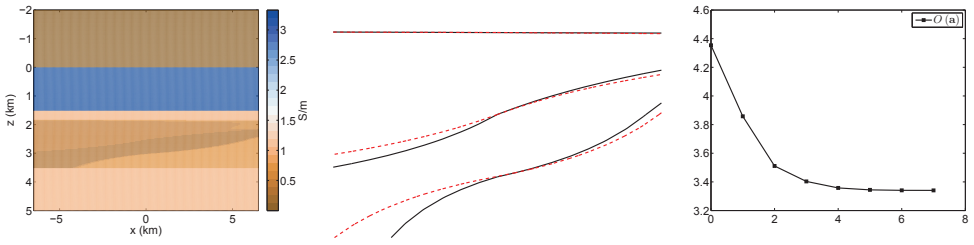

(a) (b) (c)

Fig. 12. Inversion result of test case 3 using only observed data: (a) final model, (b) I_1^0, I_2^0 and I_3^0 of final model (solid black) and reference model (dashed red), (c) log-objective function value versus iteration count.

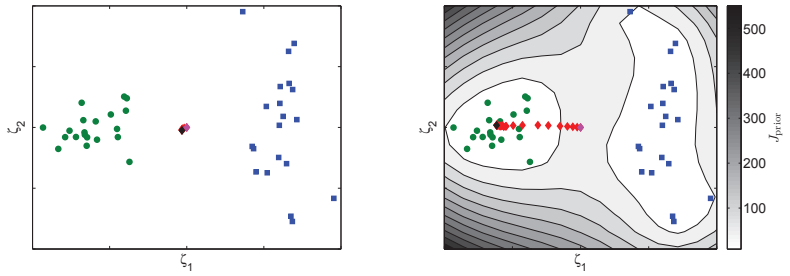

(a) (b)

Fig. 13. Test case 3. Projection onto the first two principal components (ζ_1 and ζ_2) of the training data set. Pinchout training data subset (blue squares); training data subset similar to the reference model (green circles), and; evolution of $\mathbf{a}^k$ during inversion with: (a) observed data only, (b) observed data with shape prior regularization (contours of J_{prior} are also shown). Iterates are shown as red diamonds, but with the first iteration in magenta and the last iteration in black.

data misfit has been reduced by approximately an order of magnitude. This is due to the upper half of the final model being reasonably close to the reference model as seen in Fig. 12b.

Even though we do not involve the shape prior term in this inversion, it is still interesting to see how the inversion progressed compared to the two structure types in the training data. To visualize the evolution of $\mathbf{a}^k$ compared to the training data (both in $\mathbb{R}^{N_{\text{a}}}$), we use the first two principal components of a linear principal component analysis (PCA). (Not to be confused with kPCA. We are only interested in reducing the dimensionality of $\mathbf{a}^k$ and the training data for visualization purposes.) The principal components are made from the training data, and we subsequently project $\mathbf{a}^k$ for each iteration onto the principal components. Keep in mind that the first principal components will only account for largest variation in the data, and thus give a rough representation of how the training data and $\mathbf{a}^k$ are distributed in $\mathbb{R}^{N_{\text{a}}}$. As discussed above, the final model is not much different from the initial guess, which is also indicated in Fig. 13a. Moreover, we see that the final model from the inversion is far from the two structures in the training data.

Inversion of observed data with shape prior

In this test case, we change the exponent in the power kernel (44) from $\tau = 1.5$ to $\tau = 1.75$ and decrease the regularization parameter β by a factor $\gamma = 0.8$. We chose a high τ (recall that $\tau = 2$ is the upper limit

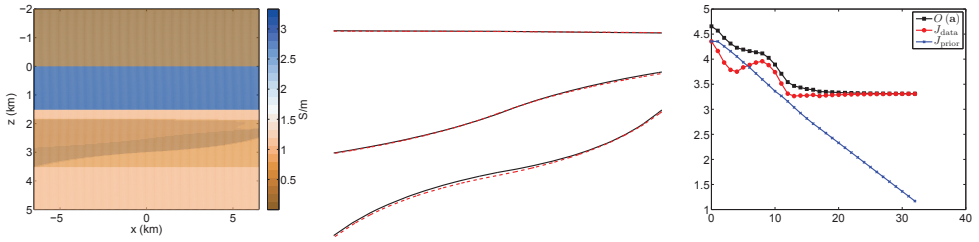

(a) (b) (c)

Fig. 14. Inversion result of test case 3 using observed data with shape prior regularization: (a) final model, (b) I_1^0, I_2^0 and I_3^0 of final model (solid black) and reference model (dashed red), (c) log-objective function values versus iteration count.

for the power kernel) to ensure that the gradient of J_{prior} around the initial model was small, and we reduce β by a larger factor since we are relatively close to the reference model.

We see from Fig. 14a and 14b that the final model is almost an exact match to the reference solution. An interesting observation can be made from the evolution of the objective function value; c.f. Fig. 14c. The data misfit term, J_{data}, is increasing from iteration 4 to 8 before it turns and decreases again from 8 to 13. This can be an indication of multiple local minima in J_{data}, highlighting the need for additional prior information to approach the global minimum.

In Fig. 13b, we show the evolution of $\mathbf{a}^k$ compared to the training data by using linear PCA, as we did for the inversion of observed data alone. We see that $\mathbf{a}^k$ clearly moves towards the cluster of structures similar to the reference solution, and the final result is in the middle of the correct cluster.

5.4. Test case 4: More complex four-layer model with two training data sets

In this test case, we introduce finer-scale variation in the four-layer reference model used in test case 2 and 3. The reference model in this test case was made using 3 interior functions with 81 interior coefficients each, and is shown in Fig. 15a. The conductivity values are the same for the four layers as given in test case 2. Since we use less interior coefficients (9 per interior function) in the inversion, it will be impossible to recover the finer scale details in the reference model.

We use the same two sets of training data as in test case 3, hence, each training data set member also vary on a coarser scale than the reference model does. This reflects a situation where the prior information from seismic interpretations does not have sufficient resolution to accurately model the geoelectric variability in the subsurface. We are then interested in assessing whether or not use of a coarse-resolution prior model is helpful in identifying the coarse-scale trends in the reference solution. Comparing the training data with the reference model, we see that the training data set in Fig. 15b approximates the reference model better than the pinchout training data set in Fig. 15c. The initial model is, as in test case 3, chosen as the mean of the entire training data set; see Fig. 11b.

Inversion of observed data

Fig. 16a and 16b show the final model. Compared to the initial model (see Fig. 11b) we see that only the bottom boundary layer has changed, and the final model and initial model are quite similar. Similarly as for test case 3, we plot the evolution of the first two principal components of $\mathbf{a}^k$ for each iteration, and compare to the training data (Fig. 17a). This plot indicates that $\mathbf{a}^k$, although slightly approaching the correct training data set, remains very close to the initial guess.

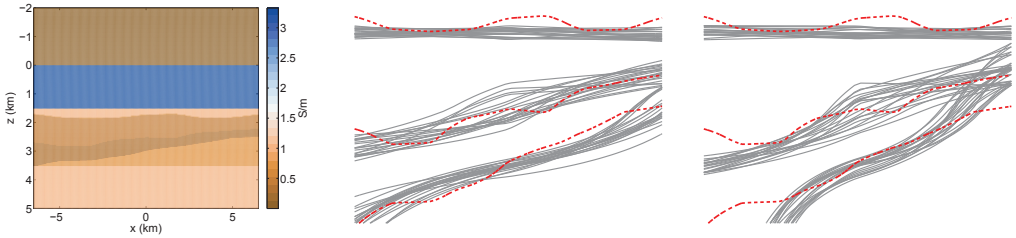

Fig. 15. Test case 4: (a) reference model, (b) and (c) the two sets of training data (grey), and I_1^0, I_2^0 and I_3^0 for the reference model (dashed red).

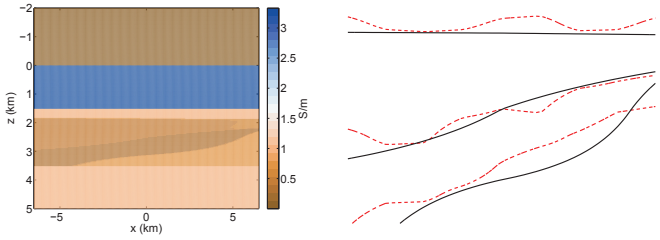

Fig. 16. Inversion result of test case 4 using only observed data: (a) final model, (b) I_1^0, I_2^0 and I_3^0 of final model (solid black) and reference model (dashed red).

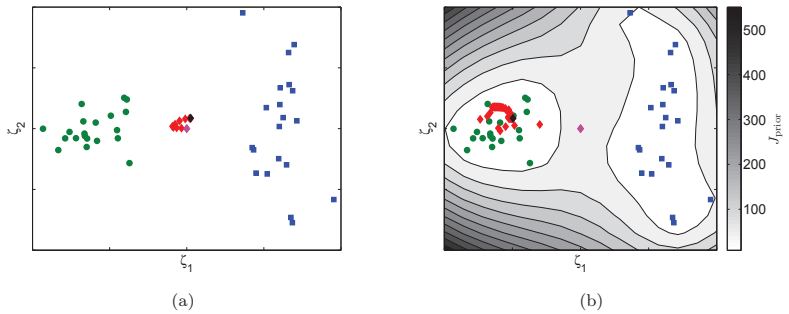

Fig. 17. Test case 4. Projection onto the first two principal components (ζ_1 and ζ_2) of the training data set. Pinchout training data subset (blue squares); training data subset similar to the reference model (green circles), and; evolution of $\mathbf{a}^k$ during inversion with: (a) observed data only; and (b) observed data with shape prior regularization (contours of J_{prior} are also shown). Iterates are shown as red diamonds, but with the first iteration in magenta and the last iteration in black.

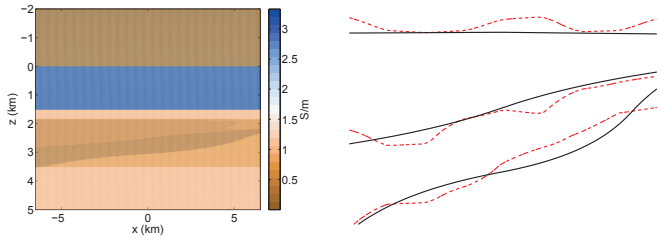

Fig. 18. Inversion result of test case 4 using observed data with shape prior regularization: (a) final model, (b) I_1^0, I_2^0 and I_3^0 of final model (solid black) and reference model (dashed red).

Inversion of observed data with shape prior

The final result of the inversion of observed data with shape prior regularization is shown in Fig. 18a and 18b. Comparing Fig. 16b and 18b, it is seen that the final estimate obtained with shape prior regularization better approximates the bottom boundary than the estimate obtained without shape prior regularization. Some improvement in the left half of the middle layer is also observed. Since the reference solution is unattainable with the applied number of parameters, the objective function value (not plotted) does not decrease nearly as much (although more than when no prior model was applied) as for the other test cases during the inversion, as expected. The progression of $\mathbf{a}^k$ compared to the training data is shown in Fig. 17b. As in test case 3, we see that $\mathbf{a}^k$ moves towards the cluster of structures similar to the reference solution, and the final model is in the middle of the cluster.

6. Summary and conclusions

We have presented a methodology for inversion of controlled source electromagnetic (CSEM) data that allows for identification of large-scale geoelectric structures with weak conductivity contrasts (corresponding, e.g., to different brine-saturated geological strata). The inversion methodology applies two types of regularization; reduced parameterization, and structural prior information. We represent the structural subsurface electric conductivity distribution with a parameterization with similarities to a level set representation, which is very flexible with respect to the shapes of the structures it can represent. Compared to a pixel-based parameterization, a level set parameterization increases nonlinearities in the mapping from parameters to model output, which is challenging for any gradient-based optimization algorithm. This increase in model nonlinearities is, however, alleviated in our parameterization by using smoothing of exterior functions and reduced representation of interior functions, reducing the risk of getting trapped in local minima when applying gradient-based optimization. Moreover, the reduced representation uses a parameter grid which is detached from the forward model grid, allowing for implementations of large models in terms of forward-model grid cells using a low number of parameters. Consequently, Gauss-Newton-type optimization methods can be used with a reduced representation, which is usually not possible with a pixel-based representation due to high computational costs associated with the Hessian matrix. Contrary to a pixel-based representation, the selected representation facilitates use of shape priors to incorporate structural prior information, potentially originating from geological interpretations of seismic data, in the CSEM inversion. Shape priors handle non-gaussian prior distributions well, which is essential, since structural prior information typically comes in the form of non-gaussian probability distributions. The numerical experiments showed that in some cases, geoelectric structures with weak conductivity contrasts can be approximately identified from CSEM data when regularizing the problem only with reduced representation. Use of shape priors clearly improved the results, however, and in test case 2, shape priors had to be introduced in order to obtain

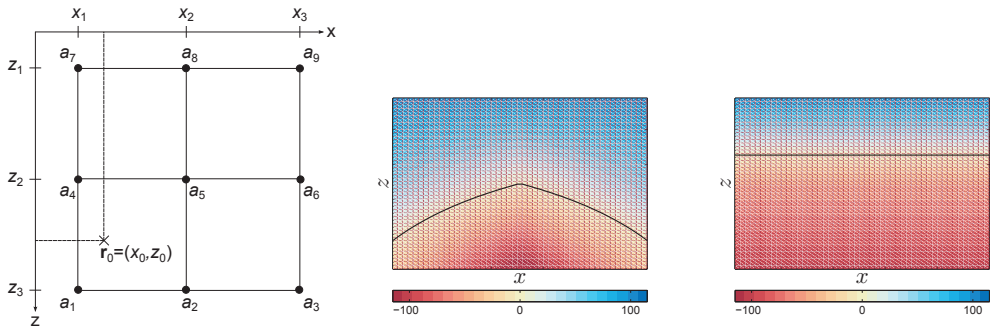

(a) (b) (c)

Fig. A.19. (a) Parameter grid with $\mathbf{r}_0$ indicated; (b) $I_1(\mathbf{r};\mathbf{a}_1)$ and I_1^0 (solid line); and (c) Example 2. $I_2(\mathbf{r};\mathbf{a}_2)$ and I_2^0 (solid line)

even an approximate identification. Use of shape priors, in addition to reduced representation, is therefore recommended.

We have assumed that the **c**-coefficients (conductivity values) are known during the inversion and independent of the spatial coordinates. This seems a natural first step when the focus is on identification of subsurface structures. We have, however, made some preliminary numerical investigations where the **c**-coefficients (still independent of the spatial coordinates) have been included as parameters during the inversion with shape priors. For this investigation, we equipped the **c**-coefficients with prior models where the standard deviations reflected that the probability of changing the internal ordering of their numerical values during the inversion should be low. Simultaneous estimation of **a** and **c** then led to similar results as those presented in the paper for all cases except test case 2, where a poor estimation of the structures was obtained. Sequential estimation (first **a**, then **c**) led to a similar result as that presented in the paper, also for test case 2.

7. Acknowledgments

The first author is grateful for the financial support by VISTA - a basic research program funded by Statoil, conducted in close collaboration with The Norwegian Academy of Science and Letters. The second author acknowledges the partial financial support from Uni CIPR. The third and fourth author are grateful for the financial support by SUCCESS centre for CO_2 storage. SUCCESS is a consortium with partners from industry and science, under grant 193825/S60 from the Research Council of Norway.

Appendix A. Two examples applying the reduced, smoothed level set representation

The general procedure for calculating q at any point $\mathbf{r} \in D$ is: first determine the parameter element containing $\mathbf{r}$, and calculate the values of the bilinear basis functions with support on this element at $\mathbf{r}$, using (27). Next, evaluate the interior functions, $\{I_i\}_{i=1}^{N_\mathrm{I}}$, at $\mathbf{r}$ from (26) with the current values of $\{\mathbf{a}_i\}_{i=1}^{N_\mathrm{I}}$ inserted. Then, evaluate $\tilde{H}$ for the calculated values of $\{I_i\}_{i=1}^{N_\mathrm{I}}$ from (25), and; calculate $\{\Psi_j\}_{j=1}^{N_\mathrm{c}}$, using (20) and (21), with $\tilde{H}$ replacing H in (21). Finally, insert $\{\Psi_j\}_{j=1}^{N_\mathrm{c}}$ and the associated exterior coefficients into (19). For the benefit of the reader we include two examples to illustrate the general procedure.

In the first example, we let $N_\mathrm{I} = 1$ and select a 3×3 parameter grid, as illustrated in Fig. A.19a. Hence, $N = 9$, and the (only) interior function for this example is then

$$I_1(\mathbf{r};\mathbf{a}_1) = a_1^1\theta_1(\mathbf{r}) + a_2^1\theta_2(\mathbf{r}) + \ldots + a_9^1\theta_9(\mathbf{r}). \tag{A.1}$$

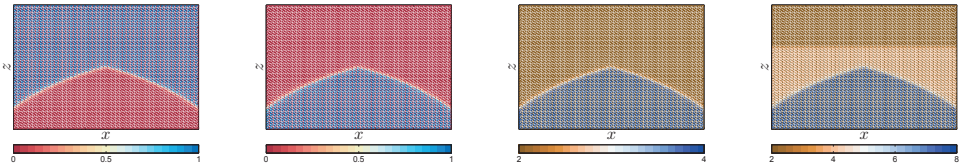

(a) (b) (c) (d)

Fig. A.20. Example 1: (a) Ψ_1; (b) Ψ_2; and (c) $q_1(\mathbf{r};\mathbf{c},\mathbf{a})$. Example 2: (d) $q_2(\mathbf{r};\mathbf{c},\mathbf{a})$

Since the bilinear basis functions are normalized, the 9 interior coefficients constitutes the values of I_1 on the parameter nodes. To calculate I_1 at a given position, say $\mathbf{r}_0 = (x_0, z_0)$, we observe from Fig. A.19a that $\mathbf{r}_0$ is located in the parameter element defined by $[x_1, x_2] \times [z_2, z_3]$. Only the basis functions $\{\theta_1, \theta_2, \theta_4, \theta_5\}$ have support on this element, hence

$$I_1(\mathbf{r}_0;\mathbf{a}_1) = a_1^1\theta_1(\mathbf{r}_0) + a_2^1\theta_2(\mathbf{r}_0) + a_4^1\theta_4(\mathbf{r}_0) + a_5^1\theta_5(\mathbf{r}_0).$$

Specifying the interior coefficients as $\mathbf{a}_1 = [-25,-125,-25,50,0,50,100,100,100]^T$, and following the above procedure for calculating $I_1(\mathbf{r};\mathbf{a}_1)$ for each $\mathbf{r}$ on the forward-model grid in D, the interior function illustrated in Fig. A.19b is obtained. Since $N_c = 2^{N_I} = 2^1 = 2$, (19) reduces to (23) and $\Psi_j \equiv E_j; \quad j = 1, 2$. Inserting I_1 into (25) and substituting $\tilde{H}$ for H in (21), one obtains Ψ_1 (Fig. A.20a), and Ψ_2 (Fig. A.20b) from (20). Inserting these basis functions, along with $\mathbf{c} = [2,4]^T$, into (23), the parameter function, q_1, illustrated in Fig. A.20c is obtained.

For the second example, we keep the same parameter grid as in the first example, but we let $N_I = 2$. We also keep I_1 as in the first example. For the second interior function, I_2, we let the interior coefficients be given as $\mathbf{a}_2 = [-100,-100,-100,-50,-50,-50,100,100,100]^T$ (Fig. A.19c). To calculate the exterior functions, we first observe that $N_c \leq 2^{N_I} = 2^2 = 4$. Thus, there can be up to 4 exterior functions with non-vanishing support, and we need to evaluate b_j^i for $j = 1,2,3,4$ and $i = 1,2$,

$$\begin{bmatrix} \text{bin}(0) \\ \text{bin}(1) \\ \text{bin}(2) \\ \text{bin}(3) \end{bmatrix} = \begin{bmatrix} b_1^1 & b_1^2 \\ b_2^1 & b_2^2 \\ b_3^1 & b_3^2 \\ b_4^1 & b_4^2 \end{bmatrix} = \begin{bmatrix} 0 & 0 \\ 0 & 1 \\ 1 & 0 \\ 1 & 1 \end{bmatrix}.$$

To evaluate the exterior functions, we invoke (21) with $\tilde{H}$ substituted for H,

$$\begin{aligned} E_1(I_1) = E_2(I_1) &= \tilde{H}(I_1), \\ E_1(I_2) = E_3(I_2) &= \tilde{H}(I_2), \\ E_2(I_2) = E_4(I_2) &= \left(1 - \tilde{H}(I_2)\right), \\ E_3(I_1) = E_4(I_1) &= \left(1 - \tilde{H}(I_1)\right), \end{aligned}$$

while the corresponding basis functions in the expansion for q are given by (20) with $\tilde{H}$ inserted for H,

$$\Psi_1 = \tilde{H}(I_1)\,\tilde{H}(I_2), \tag{A.2}$$

$$\Psi_2 = \tilde{H}(I_1)\left(1 - \tilde{H}(I_2)\right), \tag{A.3}$$

$$\Psi_3 = \left(1 - \tilde{H}(I_1)\right)\tilde{H}(I_2), \tag{A.4}$$

$$\Psi_4 = \left(1 - \tilde{H}(I_1)\right)\left(1 - \tilde{H}(I_2)\right). \tag{A.5}$$

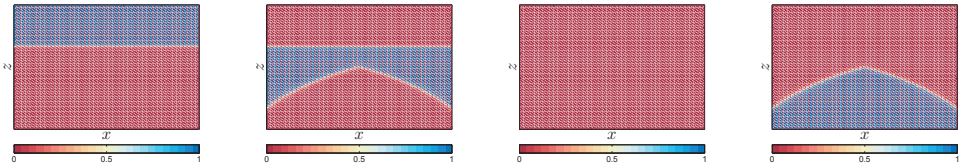

(a) (b) (c) (d)

Fig. A.21. Example 2: (a) Ψ_1; (b) Ψ_2; (c) Ψ_3; and (d) Ψ_4

Inserting I_1 and I_2 into (A.2) – (A.5), the basis functions illustrated in Fig. A.21 are obtained. Defining the exterior coefficients $\mathbf{c} = [2, 4, 6, 8]^T$, we obtain q_2 (Fig. A.20d). Since I_1^0 and I_2^0 do not intersect, the support of one of the basis functions (in this case, Ψ_3) vanishes, resulting in q_2 displaying 3 distinct regions instead of $2^{N_\mathrm{I}} = 2^2 = 4$ regions.

Appendix B. Sensitivity calculations

The entries in the sensitivity matrix $\mathbf{S}$ are

$$\mathbf{S} = \left[\frac{\mathrm{d}\mathbf{m}_i(\mathbf{a})}{\mathrm{d}\mathbf{a}_j}\right]_{i,j} = \frac{\mathrm{d}\mathbf{m}}{\mathrm{d}\mathbf{a}}. \tag{B.1}$$

$\mathbf{S}$ is a $N_\mathrm{d} \times N_\mathrm{a}$ matrix, which is found using the direct (or gradient simulator) method at each iteration k, see, e.g., [47]. In the direct method we differentiate $\mathbf{m}$ directly with $\mathbf{a}$. In the inverse problem, $\mathbf{m}$ is not readily available as an expression; it is found numerically. Thus to find $\mathrm{d}\mathbf{m}/\mathrm{d}\mathbf{a}$ we differentiate (5) with respect to $\mathbf{a}$ to get

$$\nabla \times \left(\mu^{-1}\nabla \times \frac{\partial \mathbf{E}}{\partial a_j}\right) - \mathrm{i}\omega q \frac{\partial \mathbf{E}}{\partial a_j} = \mathrm{i}\omega \frac{\partial q}{\partial a_j}\mathbf{E}, \tag{B.2}$$

where we have substituted σ in (5) with q to emphasize that this represents the reparameterized conductivity distribution. Comparing (B.2) with (5) we see that they are similar in form. Hence the resulting linear system from the 2.5D procedure on (B.2) has the same stiffness matrix $\mathbf{A}$ as in (12), which saves computational time when calculating the sensitivity matrix.

A part of (B.2) is to calculate $\partial q/\partial \mathbf{a}$ and this can be done analytically. We first note that

$$\frac{\partial q}{\partial \mathbf{a}} = \left[\frac{\partial q}{\partial a_1^1}, \ldots, \frac{\partial q}{\partial a_{N_\mathrm{a}^1}^1}, \ldots, \frac{\partial q}{\partial a_1^{N_\mathrm{I}}}, \ldots, \frac{\partial q}{\partial a_{N_\mathrm{a}^{N_\mathrm{I}}}^{N_\mathrm{I}}}\right]^T, \tag{B.3}$$

is a $N_\mathrm{g} \times N_\mathrm{a}$ matrix. To calculate an element in (B.3), we use the chain rule

$$\frac{\partial q}{\partial a_k^l} = \frac{\partial q}{\partial E_j}\frac{\partial E_j}{\partial I_l}\frac{\partial I_l}{\partial a_k^l}. \tag{B.4}$$

Starting from the back, we differentiate the interior function (26) with respect to a_k^l

$$\frac{\partial I_l}{\partial a_k^l} = \theta_k^l(\mathbf{r}). \tag{B.5}$$

This is just the bilinear basis function associated with the interior coefficient a_k^l.

Next, we differentiate the exterior function (21), using the smooth Heaviside function (25), with respect to the interior function

$$D_j\left(I_l\right) \equiv \frac{\partial E_j}{\partial I_l} = \begin{cases} \tilde{\delta}\left(I_l\right), & \text{if } b_j^i = 0, \\ -\tilde{\delta}\left(I_l\right), & \text{if } b_j^i = 1, \end{cases} \tag{B.6}$$

where $\tilde{\delta}\left(I_l\right)$ is an approximation of the Dirac delta function. To get $\tilde{\delta}\left(I_l\right)$ we differentiate the approximate Heaviside function (25) which yields

$$\tilde{\delta}\left(I_l\right) = \frac{1}{\pi\left(1+\left(I_l\right)^2\right)}. \tag{B.7}$$

Lastly, we differentiate q with respect to E_j, using (19) and (20),

$$\begin{aligned} \frac{\partial q}{\partial E_j} &= \tfrac{\partial}{\partial E_j}\left(\textstyle\sum_{j=1}^{N_c} c_j \prod_{i=1}^{N_I} E_j\left(I_i\right)\right), \\ &= \textstyle\sum_{j=1}^{N_c} c_j \prod_{i=1, i\neq l}^{N_I} E_j\left(I_i\right). \end{aligned} \tag{B.8}$$

Finally we insert all of the above expressions into (B.4), and get

$$\frac{\partial q}{\partial a_k^l} = \sum_{j=1}^{N_c} c_j \left(\prod_{i=1, i\neq l}^{N_I} E_j\left(I_i\right)\right) \tilde{\delta}\left(I_l\right) \theta_k^l. \tag{B.9}$$

Appendix C. First and second derivative of the shape prior regularization term

To successfully implement shape priors into the Levenberg-Marquardt algorithm (45) we need the first and second derivative of J_{prior}. The gradient of J_{prior} is

$$\nabla J_{\text{prior}} = \left[\frac{\partial J_{\text{prior}}}{\partial a_1^1}, \ldots, \frac{\partial J_{\text{prior}}}{\partial a_{N_a^1}^1}, \ldots, \frac{\partial J_{\text{prior}}}{\partial a_1^{N_I}}, \ldots, \frac{\partial J_{\text{prior}}}{\partial a_{N_a^{N_I}}^{N_I}}\right]^T, \tag{C.1}$$

where the individual elements are calculated as follows

$$\begin{aligned} \frac{\partial J_{\text{prior}}}{\partial a_v^u} &= 2\sum_{k=1}^{r}\left(\sum_{i=1}^{m} \alpha_i^k \tilde{k}\left(\mathbf{t}^i, \mathbf{a}\right)\right)\left(\sum_{j=1}^{m} \alpha_j^k \frac{\partial \tilde{k}\left(\mathbf{t}^j, \mathbf{a}\right)}{\partial a_v^u}\right)\left(\lambda_k^{-1} - \lambda_\perp^{-1}\right) \\ &\quad + \lambda_\perp^{-1} \frac{\partial \tilde{k}\left(\mathbf{a}, \mathbf{a}\right)}{\partial a_v^u}. \end{aligned} \tag{C.2}$$

The second derivative of J_{prior} is a Hessian matrix where the individual elements are calculated as follows

$$\begin{aligned} \frac{\partial^2 J_{\text{prior}}}{\partial a_t^s \partial a_v^u} &= 2\sum_{k=1}^{r}\left[\left(\sum_{i=1}^{m} \alpha_i^k \frac{\partial \tilde{k}\left(\mathbf{t}^i, \mathbf{a}\right)}{\partial a_t^s}\right)\left(\sum_{j=1}^{m} \alpha_j^k \frac{\partial \tilde{k}\left(\mathbf{t}^j, \mathbf{a}\right)}{\partial a_v^u}\right)\right. \\ &\quad \left. + \left(\sum_{i=1}^{m} \alpha_i^k \tilde{k}\left(\mathbf{t}^i, \mathbf{a}\right)\right)\left(\sum_{j=1}^{m} \alpha_j^k \frac{\partial^2 \tilde{k}\left(\mathbf{t}^j, \mathbf{a}\right)}{\partial a_t^s \partial a_v^u}\right)\right]\left(\lambda_k^{-1} - \lambda_\perp^{-1}\right) \\ &\quad + \lambda_\perp^{-1} \frac{\partial^2 \tilde{k}\left(\mathbf{a}, \mathbf{a}\right)}{\partial a_t^s \partial a_v^u}. \end{aligned} \tag{C.3}$$

[1] S. Constable, Ten years of marine CSEM for hydrocarbon exploration, Geophysics 75 (5) (2010) 75A67–75A81, doi:10.1190/1.3483451.

[2] T. Smith, G. M. Hoversten, E. Gasperikova, F. Morrison, Sharp boundary inversion of 2D magnetotelluric data, Geophys. Prospect. 47 (4) (1999) 469–486, doi:10.1046/j.1365-2478.1999.00145.x.
[3] C. de Groot-Hedlin, S. Constable, Inversion of magnetotelluric data for 2D structure with sharp resistivity contrasts, Geophysics 69 (1) (2004) 78–86, doi:10.1190/1.1649377.
[4] G. M. Hoversten, G. A. Newman, Integration of multiple electromagnetic imaging and inversion techniques for prospect evaluation, in: SEG Technical Program Expanded Abstracts, New Orleans, 2006.
[5] R. Villegas, O. Dorn, M. Moscoso, M. Kindelan, Simultaneous Characterization of Geological Regions and Parameterized Internal Permeability Profiles in History Matching, in: 10th European conference on the mathematics of oil recovery (ECMOR X), Amsterdam, 2006.
[6] O. Dorn, R. Villegas, History matching of petroleum reservoirs using a level set technique, Inverse Probl. 24 (3) (2008) 035015, doi:10.1088/0266-5611/24/3/035015.
[7] A. Abubakar, T. M. Habashy, M. Li, J. Liu, Inversion algorithms for large-scale geophysical electromagnetic measurements, Inverse Probl. 25 (12) (2009) 123012, doi:10.1088/0266-5611/25/12/123012.
[8] I. Berre, M. Lien, T. Mannseth, Multi-level parameter structure identification for two-phase porous-media flow problems using flexible representations, Adv. Water Resour. 32 (12) (2009) 1777–1788, doi:10.1016/j.advwatres.2009.10.002.
[9] I. Berre, M. Lien, T. Mannseth, Identification of three-dimensional electric conductivity changes from time-lapse electromagnetic observations, J. Comput. Phys. 230 (10) (2011) 3915–3928, doi:10.1016/j.jcp.2011.02.015.
[10] A. Gribenko, M. Zhdanov, Rigorous 3D inversion of marine CSEM data based on the integral equation method, Geophysics 72 (2) (2007) WA73–WA84, doi:10.1190/1.2435712.
[11] A. Abubakar, T. M. Habashy, V. L. Druskin, L. Knizhnerman, D. L. Alumbaugh, 2.5D forward and inverse modeling for interpreting low-frequency electromagnetic measurements, Geophysics 73 (4) (2008) F165–F177, doi:10.1190/1.2937466.
[12] M. Commer, G. A. Newman, New advances in three-dimensional controlled-source electromagnetic inversion, Geophys. J. Int. 172 (2) (2008) 513–535, doi:10.1111/j.1365-246X.2007.03663.x.
[13] R.-E. Plessix, W. A. Mulder, Resistivity imaging with controlled-source electromagnetic data: depth and data weighting, Inverse Probl. 24 (3) (2008) 034012, doi:10.1088/0266-5611/24/3/034012.
[14] L. A. Gallardo, M. A. Meju, Structure-coupled multiphysics imaging in geophysical sciences, Rev. Geophys. 49 (1) (2011) RG1003, doi:10.1029/2010RG000330.
[15] M. Lien, T. Mannseth, Structural joint inversion of AVO and CSEM data using flexible representations, in: SEG Technical Program Expanded Abstracts, San Antonio, Texas, 2011.
[16] M. Lien, Simultaneous joint inversion of amplitude-versus-offset and controlled-source electromagnetic data by implicit representation of common parameter structure, Geophysics 78 (4) (2013) ID15–ID27.
[17] M. Zhdanov, A. Gribenko, G. Wilson, Generalized joint inversion of multimodal geophysical data using Gramian constraints, Geophys. Res. Lett. 39 (9) (2012) L09301, doi:10.1029/2012GL051233.
[18] D. Cremers, T. Kohlberger, C. Schnörr, Shape statistics in kernel space for variational image segmentation, Pattern Recogn. 36 (9) (2003) 1929–1943, doi:10.1016/S0031-3203(03)00056-6.
[19] B. Schölkopf, The kernel trick for distances, Adv. Neur. In. 13 (2001) 1–7.
[20] L. A. Tabarovsky, M. M. Goldman, M. B. Rabinovich, K.-M. Strack, 2.5-D modeling in electromagnetic methods of geophysics, J. Appl. Geophys. 35 (4) (1996) 261–284, doi:10.1016/0926-9851(96)00025-0.
[21] J. R. Shewchuk, Triangle: Engineering a 2D Quality Mesh Generator and Delaunay Triangulator, Applied Computational Geometry: Towards Geometric Engineering 1148 (1996) 203–222, doi:10.1007/BFb0014497.
[22] S. A. Bakr, A 2.5D finite element method for modeling of electromagnetic tensor Green's functions on a triangular mesh, Tech. rep., Uni Cipr, Bergen (2011).
[23] H. W. Engl, M. Hanke, A. Neubauer, Regularization of Inverse Problems, Kluwer Academic Publishers, Dordrecht, 2000.
[24] L. A. Vese, T. F. Chan, A multiphase level set framework for image segmentation using the Mumford and Shah model, Int. J. Comput. Vision 50 (3) (2002) 271–293, doi:10.1023/A:1020874308076.
[25] T. F. Chan, X.-C. Tai, Level set and total variation regularization for elliptic inverse problems with discontinuous coefficients, J. Comput. Phys. 193 (1) (2003) 40–66, doi:10.1016/j.jcp.2003.08.003.
[26] A. Litman, Reconstruction by level sets of n-ary scattering obstacles, Inverse Probl. 21 (6) (2005) S131–S152, doi:10.1088/0266-5611/21/6/S10.
[27] S. J. Osher, J. A. Sethian, Fronts propagating with curvature-dependent speed: Algorithms based on Hamilton-Jacobi formulations, J. Comput. Phys. 79 (1) (1988) 12–49, doi:10.1016/0021-9991(88)90002-2.
[28] X.-C. Tai, T. F. Chan, A survey on multiple level set methods with applications for identifying piecewise constant functions, Int. J. Numer. Anal. Mod. 1 (1) (2004) 25–47.
[29] O. Dorn, D. Lesselier, Level set methods for inverse scattering, Inverse Probl. 22 (4) (2006) R67–R131, doi:10.1088/0266-5611/22/4/R01.
[30] O. Dorn, D. Lesselier, Level set methods for inverse scattering - some recent developments, Inverse Probl. 25 (12) (2009) 125001, doi:10.1088/0266-5611/25/12/125001.
[31] R. Villegas, F. Mustieles, M. Kindelan, O. Dorn, M. Moscoso, Simultaneous Characterization of Geological Shapes and Permeability Distributions in Reservoirs Using the Level Set Method, in: SPE Europec/EAGE Annual Conference and Exhibition, Society of Petroleum Engineers, 2006, doi:10.2118/100291-MS.
[32] D. Adalsteinsson, J. A. Sethian, A fast level set method for propagating interfaces, J. Comput. Phys. 118 (2) (1995) 269–277, doi:10.1006/jcph.1995.1098.
[33] M. Lien, I. Berre, T. Mannseth, Combined adaptive multiscale and level-set parameter estimation, Multiscale Model. Sim. 4 (4) (2005) 1349–1372, doi:10.1137/050623152.
[34] A.-A. Grimstad, T. Mannseth, G. Nævdal, H. Urkedal, Adaptive multiscale permeability estimation, Computat. Geosci.

7 (1) (2003) 1–25, doi:10.1023/A:1022417923824.
[35] B. Schölkopf, A. Smola, K.-R. Müller, Nonlinear component analysis as a kernel eigenvalue problem, Neural Comput. 10 (5) (1998) 1299–1319, doi:10.1162/089976698300017467.
[36] N. Cristianini, J. Shawe-Taylor, An Introduction to Support Vector Machines and Other Kernel-based Learning Methods, Cambridge University Press, New York, 2000.
[37] J. Shawe-Taylor, N. Cristianini, Kernel Methods for Pattern Analysis, Cambridge University Press, New York, 2004.
[38] V. N. Vapnik, Statistical learning theory, Wiley, New York, 1998.
[39] B. Schölkopf, A. J. Smola, Learning with Kernels: Support Vector Machines, Regularization, Optimization, and Beyond, MIT Press, Cambridge, 2001.
[40] C. Scheidt, J. Caers, Representing spatial uncertainty using distances and kernels, Math.Geosci. 41 (4) (2008) 397–419, doi:10.1007/s11004-008-9186-0.
[41] P. Sarma, L. J. Durlofsky, K. Aziz, Kernel principal component analysis for efficient, differentiable parameterization of multipoint geostatistics, Math.Geosci. 40 (1) (2007) 3–32, doi:10.1007/s11004-007-9131-7.
[42] C. Berg, J. P. R. Christensen, P. Ressel, Harmonic Analysis on Semigroups: Theory of Positive Definite and Related Functions, Springer, Berlin, 1984.
[43] J. Mercer, Functions of positive and negative type, and their connection with the theory of integral equations, P. Roy. Soc. A-Math. Phy. 209 (1909) 415–446, doi:10.1098/rspa.1909.0075.
[44] D. Cremers, Statistical shape knowledge in variational image segmentation, Ph.D. thesis, Department of Mathematics and Computer Science, University of Mannheim, Germany (2002).
[45] E. Parzen, On estimation of a probability density function and mode, Ann. Math. Stat. 33 (3) (1962) 1065–1076, doi:10.1214/aoms/1177704472.
[46] R. Fletcher, A modifed Marquardt subroutine for non-linear least squares, Tech. rep., Atomic Energy Research Establishment, Harwell, England (1971).
[47] P. R. McGillivray, D. W. Oldenburg, Methods for calculating Frèchet derivatives and sensitivities for the non-linear inverse problem: A comparative study, Geophys. Prospect. 38 (5) (1990) 499–524, doi:10.1111/j.1365-2478.1990.tb01859.x.
[48] P. E. Gill, W. Murray, M. H. Wright, Practical optimization, Academic Press, 1981.
[49] G. A. Newman, G. M. Hoversten, Solution strategies for two- and three-dimensional electromagnetic inverse problems, Inverse Probl. 16 (5) (2000) 1357–1375, doi:10.1088/0266-5611/16/5/314.
[50] A. H. Flosadóttir, S. Constable, Marine controlled-source electromagnetic sounding 1. Modeling and experimental design, J. Geophys. Res. 101 (B3) (1996) 5507–5517, doi:10.1029/95JB03739.
[51] M. Zhdanov, Geophysical Inverse Theory and Regularization Problems, Elsevier, Amsterdam, 2002.